Regional Petrophysical Properties of Mesaverde Low-Permeability Sandstones

Alan P. Byrnes[1], John C. Webb[2], and Robert M. Cluff [2]

1- Kansas Geological Survey, Lawrence, KS

2- The Discovery Group, Inc., Denver, CO

http://www.kgs.ku.edu/mesaverde

KANSAS GEOLOGICAL SURVEY The University of Kansas

The Discovery Group, Inc.

Abstract

Petrophysical properties of Mesaverde Group tight gas sandstones for the range of lithofacies present in the Washakie, Uinta, Piceance, Upper Greater Green River, Wind River, and Powder River basins exhibit consistent trends among lithofacies. Grain density for 2400 samples averages 2.654±0.033 g/cc (±1sd) with grain density distributions differing slightly among basins. The Klinkenberg gas slip proportionality constant, b, can be approximated using the relation: b(atm) = 0.851 $k_{ik}^{-0.34}$. Regression provides a relation for *in situ* Klinkenberg permeability (k_{ik}): log k_{ik} = 0.282 μ_i + 0.18 RC2 - 5.13 (±4.5X,1 sd), where μ_i = *in situ* porosity, and RC2 = a size-sorting index. Artificial neural network analysis provides prediction within ±3.3X. Analysis of 700 paired samples indicates 90% of all samples exhibit porosity within 10%-20%. Permeability exhibits up to 40% variance from a mean value for 80% of samples.

Capillary pressure (Pc) exhibits an air-mercury threshold entry pressure (P_{te}) versus k_{ik} trend of P_{te} = 30.27 $k_{ik}^{-0.44}$ and wetting-phase saturation at any given Pc (for 350< Pc < 3350 psia air-Hg) and k_{ik} of S_w = A $k_{ik}^{-0.138}$ where A = -13.1*ln($Pc_{air\text{-}Hg}$)+117. Accuracy of the Leverett J function is poorer. Hysteresis Pc analysis indicates that residual nonwetting-phase saturation to imbibition (*Srnw*) increases with increasing initial nonwetting phase saturation (*Snwi*) consistent with the Land-type relation: 1/Snwr-1/Snwi = 0.55±0.2. Electrical resistivity measurements show that the Archie cementation exponent (*m*) decreases with decreasing porosity (μ) below approximately 0.06 and can be generally described by the empirical relationship: *m* = 0.95-9.2 μ +6.35 $\mu^{0.5}$. These relationships are still being investigated. The Mesaverde Project website is (http://www.kgs.ku.edu/mesaverde).

Acknowledgement

We wish to acknowledge the U.S. Department of Energy for support of this work under Contract # DE-FC26-05NT42660. Project Manager - Purna Halder

Project Overview

TITLE: ANALYSIS OF CRITICAL PERMEABLITY, CAPILLARY PRESSURE AND ELECTRICAL PROPERTIES FOR MESAVERDE TIGHT GAS SANDSTONES FROM WESTERN U.S. BASINS

DOE Contract No. DE-FC26-05NT42660

Contractor:	University of Kansas Center for Research, Inc.
DOE Program:	Natural Gas Technologies (Advanced Diagnostics & Imaging)
DOE Cost Amount:	$411,030
Program Period:	October 1, 2005 June 30, 2008
DOE Project Manager:	Purna Halder, NETL Tulsa, OK
Contractor Contact:	Alan P. Byrnes Kansas Geological Survey 1930 Constant Ave., Lawrence, Kansas 66047 email: abyrnes@kgs.ku.edu phone: 785-864-2177
Principal Investigators:	Alan P. Byrnes (Program Manager) Robert Cluff (Discovery Group) John Webb (Discovery group)

Tight gas sandstones (TGS) represent 72% (342 Tcf) of the projected unconventional resource (474 Tcf) with Rocky Mountain tight gas sandstones representing 70% of the total TGS resource base (241 Tcf; EIA, 2004). The Mesaverde Group tight gas sandstones represent a principal gas productive unit in Western U.S. basins including the basins that are the focus of this project (Washakie, Uinta, Piceance, Upper Greater Green River, Wind River). Industry assessment of the regional gas resource and exploration programs requires an understanding of the reservoir properties and accurate tools for formation evaluation of drilled wells. The goal of this project is to provide petrophysical formation evaluation tools related to relative permeability, capillary pressure, electrical properties and algorithm tools for wireline log analysis. Detailed and accurate moveable gas-in-place resource assessment is most critical in marginal gas plays. Most important is that there is clear quantitative distinction between gas that is inaccessible due to technology and gas that is inaccessible due to rock physics.

Tasks involved include collection and consolidation of published advanced rock properties data into a publicly accessible relational digital database and collection of at least 300 rock samples and digital wireline logs from 4-5 wells each from five basins that will represent the range of lithofacies present in the Mesaverde Group in these basins (Task 1). Basic properties (including routine and in situ porosity, permeability, and grain density) of these rocks will be measured and, based on these properties, 150 samples will be selected to represent the range of porosity, permeability, and lithofacies in the wells and basins (Task 2.1). Measurements to be performed on these selected samples comprise: 1) Drainage critical gas saturation (2.2), Routine and in situ mercury intrusion capillary pressure analysis (2.3), cementation and saturation exponents and cation exchange capacity using multi-salinity method (2.4), geologic properties including core description, thin-section microscopy, including diagenetic and point-count analysis (2.5), and standard wireline log analysis (2.6). The compiled published data and data measured in the study will be input to an Oracle database (3.1). XML code will be written that will provide web-based access to the data and will allow construction of rock catalog format output sheets based on user-input search and comparison criteria. The data will also be available as a complete Oracle database (3.2). Core and wireline log calculated properties will be compared and algorithms developed for improved calculation of reservoir properties from log response (Task 4). To evaluate the scale dependence of critical gas saturation bedform-scale reservoir simulation models will be constructed that represent the basic bedform architectures present in the Mesaverde sandstones. Simulations will be performed that will parametrically analyze how critical gas saturation and relative permeability scale with size and bedding architecture (Task 5). An active and aggressive web-based, publication, and short-course technology transfer program will be performed (Task 6).

This project represents a two-year collaboration of the Kansas Geological Survey at University of Kansas and The Discovery Group, Inc. The projects requests $411,030 of US Department of Energy funds over two years to support the program and technology transfer activities. The project manager is Alan P. Byrnes with the KGS (phone: 785-864-2177; email: abyrnes@kgs.ku.edu.

Representative Well and Core Sampling

Samples were obtained from cores from 4 to 13 wells in each of the six basins in the project (Washakie, Uinta, Piceance, Upper Greater Green River, Wind River, and Powder River). The wells in each basin were selected to provide a wide geographic distribution and core were sampled from the USGS core repository in Denver, Colorado and contributed from industry participants. Core plugs were selected to provide a comprehensive range in lithofacies, both reservoir and nonreservoir, characteristic of the Mesaverde in the area and basin. Sampling was also intended to represent the complete range in porosity, permeability, grain density, depth, grain size, bedding, and other lithologic characteristics.

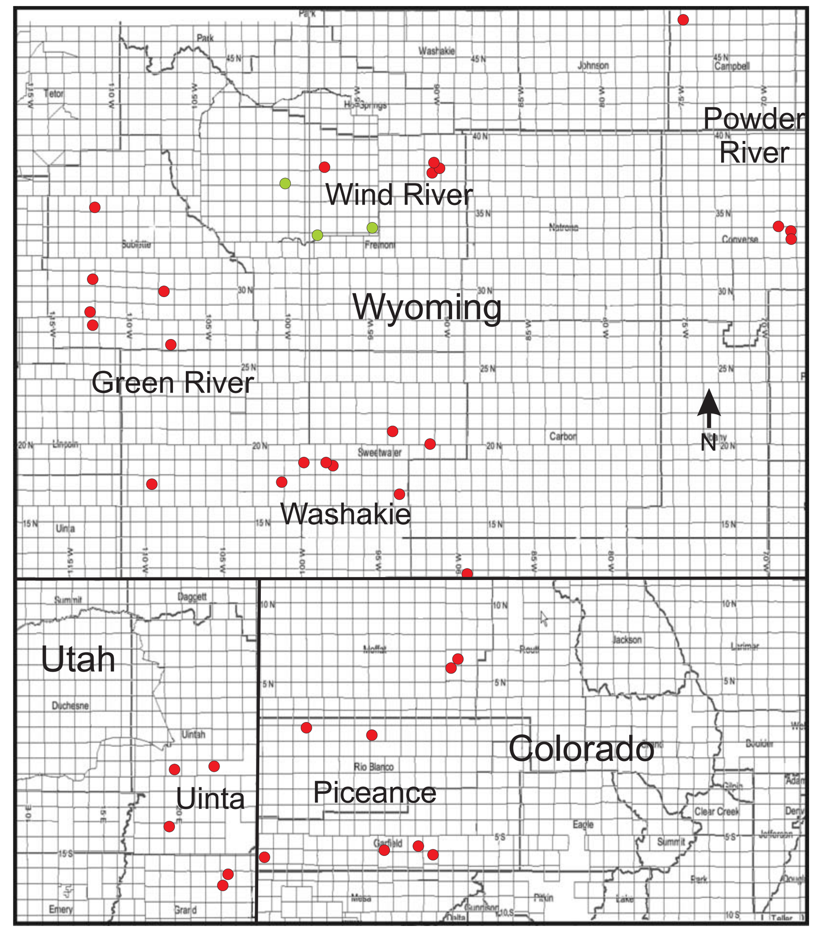

STATE CODE	COUNTY CODE	WELL	STATE	COUNTY_NAME	BASIN_NAME	FIELD_NAME	WELL_NAME	OPERATOR_NAME	TWN	TWN	RNG	RNG	SEC	SPOT
49	035	20622	WY	SUBLETTE	GREEN RIVER	WILDCAT	1 OLD ROAD	AMERICAN HUNTER EXPL	27	N	108	W	27	SENWSE
49	013	08024	WY	SUBLETTE	GREEN RIVER	PINEDALE	5 PINEDALE	EL PASO NATURAL GAS	30	N	108	W	5	C SE
49	035	20088	WY	SUBLETTE	GREEN RIVER	MERNA	A-1 WASP	INEXCO OIL COMPANY	36	N	112	W	28	NWNESW
49	035	06020	WY	SUBLETTE	GREEN RIVER	BIG PINEY	B-54 BIG PINEY	BELCO PETROLEUM	29	N	113	W	26	SESENE
49	035	05742	WY	SUBLETTE	GREEN RIVER	TIP TOP SHALLOW	C-47 TIP TOP SHALLOW	BELCO PETROLEUM	28	N	113	W	22	SWNE
49	035	06200	WY	SUBLETTE	GREEN RIVER	MASON	K-2 MASON	BELCO PETROLEUM	31	N	113	W	13	SESE
05	045		CO	GARFIELD	PICEANCE		1 BOOK CLIFFS-DRILL HOLE	USGS-CG	7	S	104	W	17	NESW
05	045	11402	CO	GARFIELD	PICEANCE	MAMM CREEK	LAST DANCE 43C-3-792	BILL BARRETT CORP.	S	7	W	92	3	NESE
05	045	06578	CO	GARFIELD	PICEANCE	GRAND VALLEY	MV 24-20 CHEVRON	BARRETT ENERGY	6	S	96	W	20	SENW
05	045	06001	CO	GARFIELD	PICEANCE	RULISON	MWX-2 SUPERIOR	CER CORPORATION	6	S	94	W	34	SESWNW
05	045	10927	CO	GARFIELD	PICEANCE	PARACHUTE	PUCKETT/TOSCO PA 424-34	WILLIAMS E&P	6	S	95	W	34	SWSE
49	035	24198	WY	GREEN	PICEANCE	PINEDALE	Vible 1B-11D	SHELL E&P	31	N	109	W	11	SENE
05	103	10391	CO	PICEANCE	PICEANCE	WILLOW RIDGE	EM T63X-2G	EXXON-MOBIL	3	S	97	W	2	NESWNE
05	103		CO	RIO BLANCO	PICEANCE	LOWER WHITE RIVER	21011-5 MOON LAKE	WESTERN FUELS ASSOC	2	N	101	W	1	NESW
05	103	09406	CO	RIO BLANCO	PICEANCE	WHITE RIVER DOME	M-30-2-96W /D-037934	FUEL RESOURCES DEV	2	N	96	W	30	SWSW
49	005	25627	WY	CAMPBELL	POWDER RIVER	BRIDGE DRAW	1 BARLOW 21-20	LOUISIANA LAND & EXP	48	N	75	W	20	NENW
49	009	21513	WY	CONVERSE	POWDER RIVER	MIKES DRAW	2 FRED STATE	DAVIS OIL COMPANY	35	N	70	W	36	NESESW
49	009	06335	WY	CONVERSE	POWDER RIVER	FLAT TOP	2 SHAWNEE	BELCO PETROLEUM	33	N	69	W	2	NENW
49	009	05481	WY	CONVERSE	POWDER RIVER	FLAT TOP	3 SHAWNEE	BELCO PETROLEUM	33	N	69	W	23	C SENE
05	081	06718	CO	MOFFAT	SAND WASH	WEST CRAIG	1-691-0513	COCKRELL OIL CORP	6	N	91	W	5	SESWSW
05	081	06724	CO	MOFFAT	SAND WASH	CRAIG DOME	1-791-2613	COCKRELL OIL CORP	7	N	91	W	26	NESWSW
43	047	30584	UT	UINTAH	UINTA	NATURAL BUTTES	11-17F RIVER BEND UNIT	MAPCO INCOPORATED	10	S	20	E	17	SENENW
43	019		UT	GRAND	UNITA		3 BOOK CLIFFS	USGS-CG	17	S	24	E	3	SE
43	019		UT	GRAND	UNITA		4 BOOK CLIFFS	USGS-CG	17	S	24	E	31	NWSW
43	047	30545	UT	UINTAH	UNITA	BONANZA	2-7 FLAT MESA FEDERAL	ENSERCH EXPLORATION	10	S	23	E	7	NESENW
43	047	30860	UT	UINTAH	UNITA	WILDCAT	3-24 US LAMCO	CHAMPLIN PETROLEUM	13	S	20	E	24	SWNESE
43	047	30584	UT	UINTAH	UNITA	AGENCY DRAW	4-5 US LAMCO	ENSERCH EXPLORATION	13	S	20	E	5	WSW
43	047	36565	UT	UINTAH	UNITA	NATURAL BUTTES	NBU 1022-1A	KERR-MCGEE OIL&GAS ONSHORE	10	S	22	E	1	SWSE
46	047	36401	UT	UINTAH	UNITA	NATURAL BUTTES	NBU 920-36O	KERR-MCGEE OIL&GAS ONSHORE	9	S	22	E	36	SWSE
49	007	21170	WY	CARBON	WASHAKIE	SAVERY	C-11 /FEE	FUEL RESOURCES DEV	12	N	90	W	11	NENW
49	037	21075	WY	SWEETWATER	WASHAKIE	WILD ROSE	1 CHAMPLIN 237 AMOCO C	AMOCO PRODUCTION	17	N	94	W	5	SWNESW
49	037	05405	WY	SWEETWATER	WASHAKIE	CHIMNEY ROCK	1 CHIMNEY ROCK	MOUNTAIN FUEL SUPPLY	18	N	102	W	12	SESW
49	037	21053	WY	SWEETWATER	WASHAKIE	FIVE MILE GULCH	3 UNIT	AMOCO PRODUCTION	21	N	93	W	35	C SW
49	037	23956	WY	SWEETWATER	WASHAKIE	SIBERIA RIDGE	5-2 SIBERIA RIDGE UNIT	AMOCO PRODUCTION	21	N	94	W	5	SW
49	037	05683	WY	SWEETWATER	WASHAKIE	PATRICK DRAW	65-1-7 ARCH UNIT	FOREST OIL CORP	19	N	99	W	1	NWSE
49	037	05577	WY	SWEETWATER	WASHAKIE	ARCH	ARCH UNIT UPRR #102-7-10	ANADARKO E&P CO. LP	19	N	98	W	7	SWSW
49	037	05349	WY	SWEETWATER	WASHAKIE		B-2A SPIDER CREEK	HUMBLE OIL & REF	18	N	110	W	27	NESW
49	037	26493	WY	SWEETWATER	WASHAKIE	WILD ROSE	CHAMPLIN 261-A13	BP AMERICA PRODUCTION, INC.	18	N	94	W	33	SENE
49	037	22304	WY	SWEETWATER	WASHAKIE	DRIPPING ROCK	DRIPPING ROCK #3	CELSIUS	14	N	94	W	8	SWNW
49	037	22355	WY	SWEETWATER	WASHAKIE	DRIPPING ROCK	DRIPPING ROCK #5	CELSIUS	14	N	94	W	19	SWNE
49	013	20966	WY	FREMONT	WIND RIVER	MADDEN	1-27 LOOKOUT	MONSANTO OIL	38	N	91	W	1	SWNENW
49	013	20786	WY	FREMONT	WIND RIVER	LYSITE	1-9 LYSITE	MICH WISC PIPELINE	38	N	91	W	9	SWNE
49	013	20836	WY	FREMONT	WIND RIVER	MADDEN	2-1 CHEVRON	MONSANTO OIL	39	N	91	W	27	CSWNE
49	013	20724	WY	FREMONT	WIND RIVER		31-22 TRIBAL PHILLIPS	BROWN TOM INC	4	N	3	E	31	NWSENW

Grain Density

Grain density distribution for the samples measured average 2.654+0.033 g/cc (error bar is 1 standard deviation). Grain density distribution is skewed slightly to high density reflecting variable concentration of calcite, dolomite, and rare pyrite cement. Grain densities for the wells sampled exhibit a slight difference in distribution between basins. It is important to note the small sample population of the Powder, Sand Wash and Wind River Basin samples and these may be biased for conditions in a few wells and intervals.

	All Basins	Green River	Piceance	Powder River	Sand Wash	Uintah	Wind River	Washakie
mean	2.654	2.645	2.663	2.679	2.633	2.646	2.672	2.662
median	2.652	2.641	2.662	2.674	2.639	2.648	2.673	2.661
stdev	0.033	0.028	0.035	0.026	0.020	0.031	0.029	0.034
min	2.505	2.505	2.528	2.599	2.593	2.522	2.515	2.511
max	2.853	2.770	2.801	2.747	2.672	2.770	2.727	2.853
kurtosis	3.323	3.517	3.333	3.928	0.173	3.358	10.378	4.054
skew	0.031	0.353	-0.250	-0.284	-0.568	-0.800	-2.045	0.526
count	1611	488	267	28	27	378	77	373

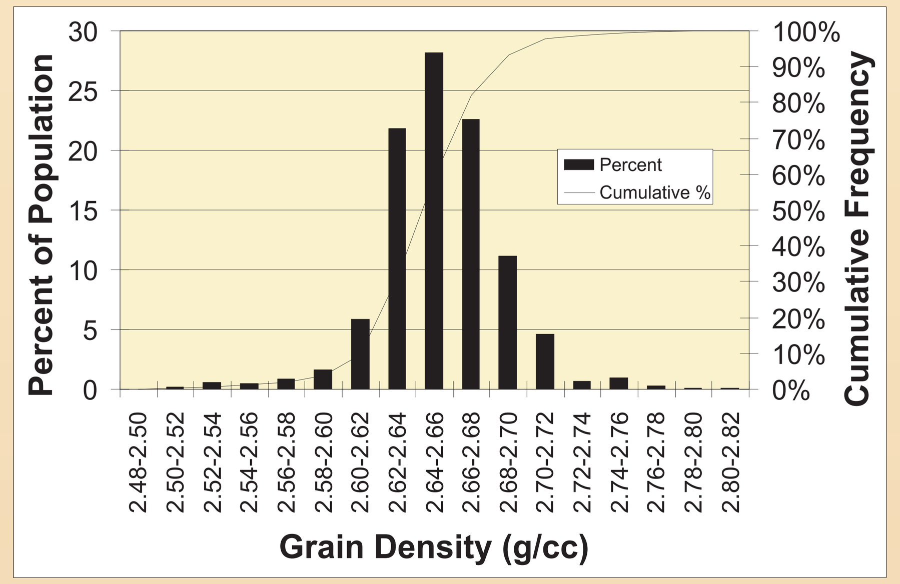

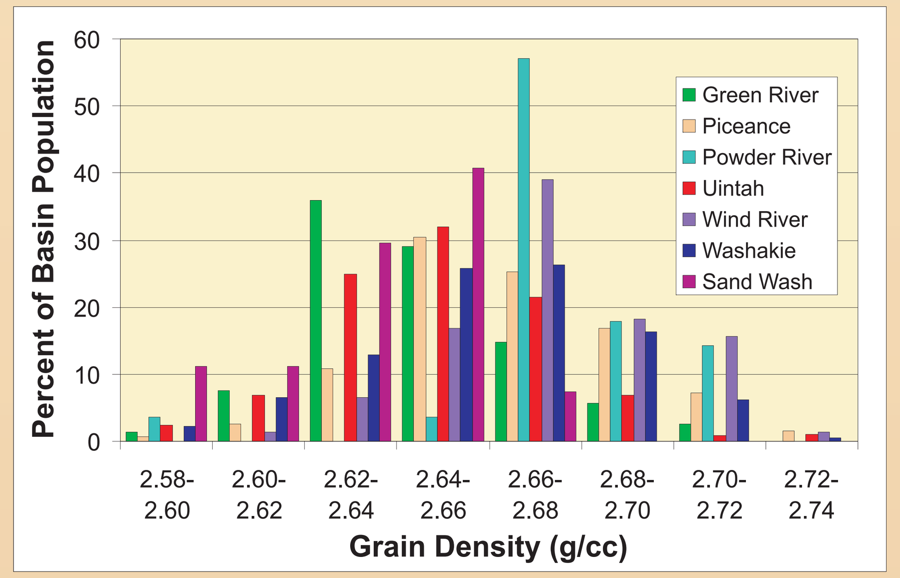

Plug Pairs

For over 800 samples core plugs greater than 3 inches in length were cut in half to provide two paired core plugs for advanced properties measurements. Figure 1 illustrates the ratio of helium porosities of samples to the mean porosity of the sample pair. Over 75% of all samples exhibit porosity within 10% of the mean porosity of the porosity pair, and 88% exhibit porosities within 20%. Figure 2 illustrates the ratio of in situ Klinkenberg permeabilities of samples to the geometric mean permeability of the sample pair. Approximately 35% of all samples exhibit a permeabilities within 10% of the mean, 55% within 20%, 70% within 30%, and 80% within 40%.

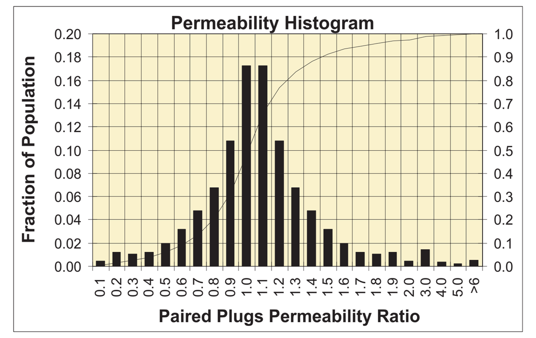

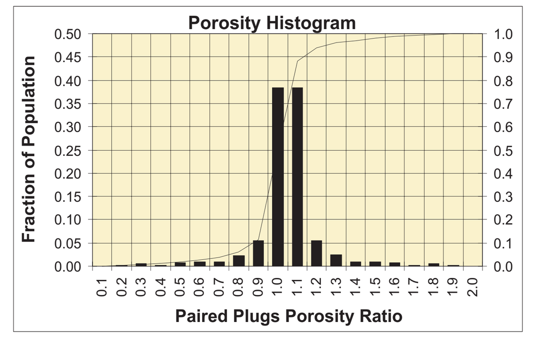

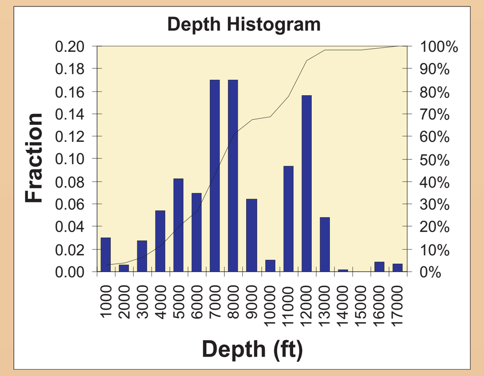

Core samples represent a wide range of depths in all basins

Porosity

The porosity distribution of the core samples analyzed to date is skewed to lower porosity consistent with general porosity distribution in the Mesaverde sandstone. The large population of cores with porosity of μ=0-2% partially reflects a heavy sampling of low porosity intervals in two Green River Basin wells. These distributions represent the sample database and do not necessarily represent basin properties.

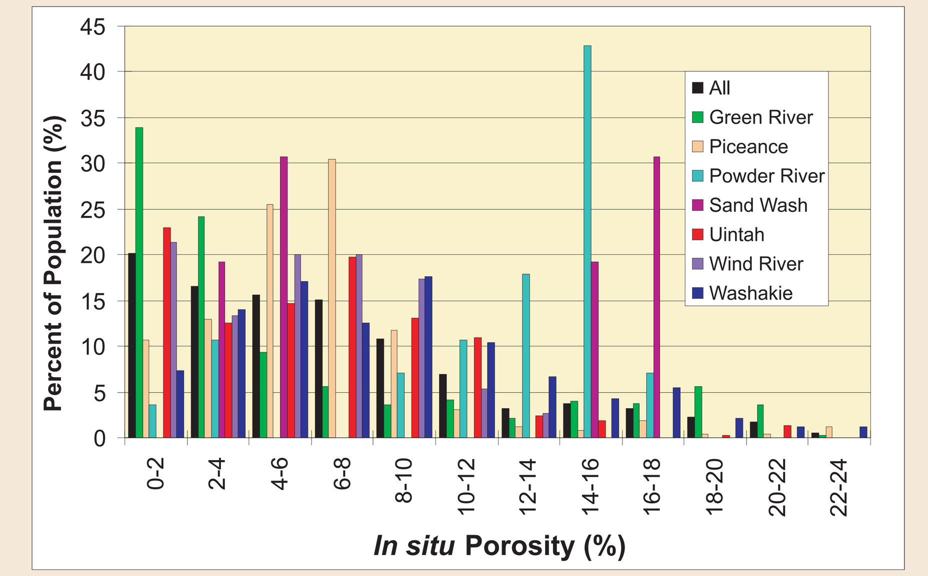

Permeability

Permeability for the samples analyzed is approximately log-normally distributed with 52% of the sample exhibiting *in situ* Klinkenberg permeability (kik) in the range 0.0001-0.01 mD and 18% of the samples exhibiting kik < 0.0001 mD and 30% exhibiting kik>0.01 mD. The distribution of permeability for samples from different basins is generally similar though slight differences in the mean and standard deviation exist. These distributions are for the sample set and may not reflect actually distributions within the basins.

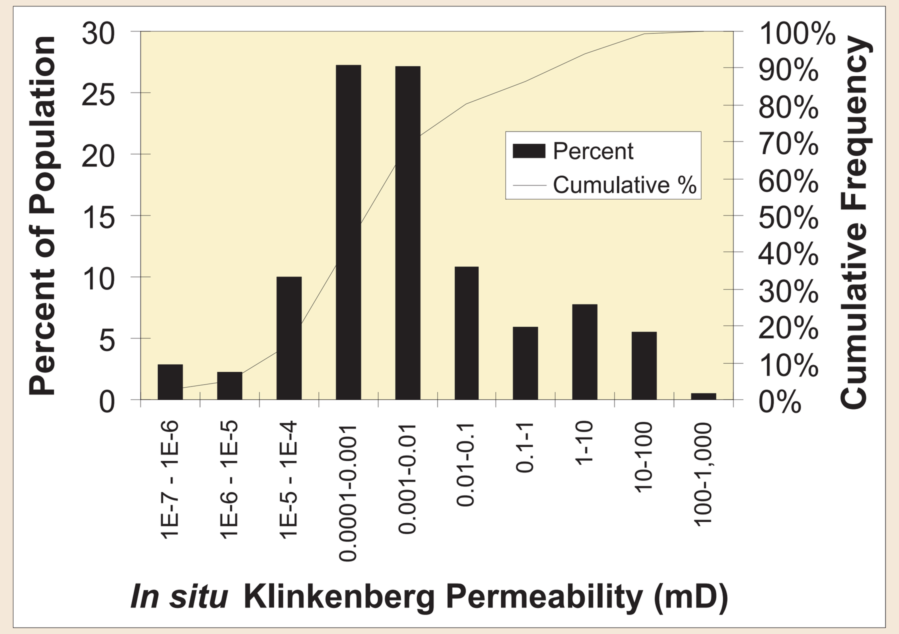

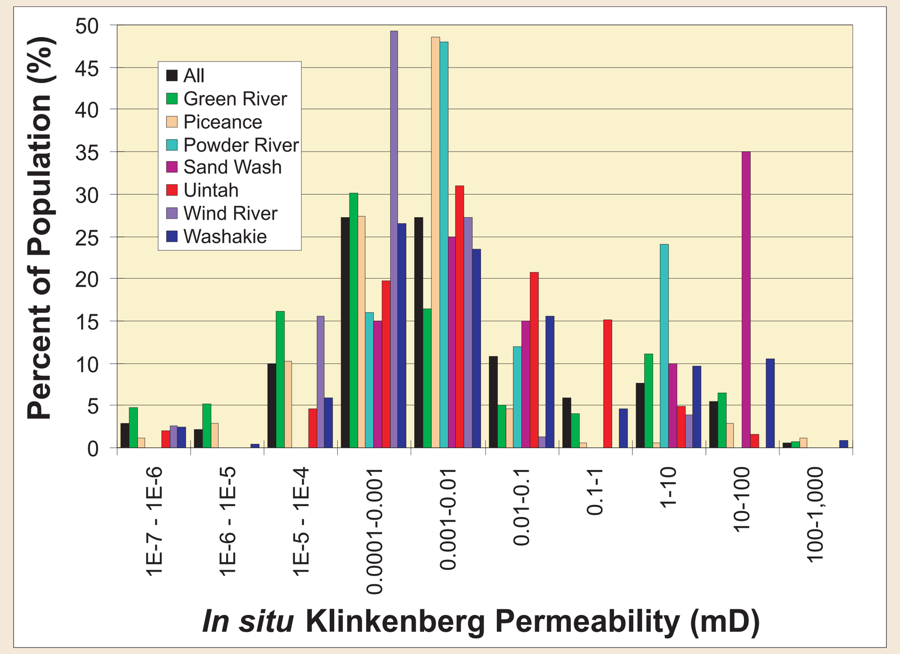

Byrnes, Alan P., John C. Webb, and Robert M. Cluff, 2007, "Regional petrophysical properties of Mesaverde low-permeability sandstones", Proceedings of the American Assoc. Of Petroleum Geologists Rocky Mountain Section Meeting, October 7-9, Snowbird, UT. (Panel 1)

Digital Rock Classification

Approximately 2500 net feet of core from 44 wells are described. All core intervals and samples collected for petrophysical analysis were classified using a five number digital code (e.g. 12345) which encodes grain size/sorting, consolidation, sedimentary structure, and mineralogy of pore filling materials.

Rock typing compresses most significant lithologic variations into a simple code and allows grouping of petrophysical data along natural lines. It is objective and independent of any interpretations of depositional environments or stratigraphic position.

Shaly intervals of the Mesaverde Group are dominated by mudstones and silty shales (rock types 10x19 and 11x29), lenticular and wavy bedded very shaly sandstones (12x3x and 12x4x), and wavy bedded to ripple cross-laminated shaly sandstones (13x4x and 13x6x).

Sandstone intervals are dominated by ripple cross-laminated and cross-bedded, very fine to fine grained sandstones (rock types 14x6x, 14x7x), low angle cross-laminated to planar laminated sandstones (14x8x), and massive sandstones (14x9x). Medium grained sandstones are mostly restricted to the Upper Almond (15x7x and 15x9x).

Table 1. Basic macroscopic rock description digital classification system showing digits of relevance to present study.

MAJOR GROUPS
0xxxx Organic rocks (coals, etc.)
1xxxx Siliciclastic rocks
SECOND DIGIT: Grain size, sorting, texture
10xxx Shales
11xxx Silty shales (60-90% clay)
12xxx Siltstones or very shaly sandstones (40-65% clay and silt)
13xxx Moderately shaly sandstones (10-40% clay and silt)
14xxx Sandstones, fine to very fine
15xxx Sandstones, medium
16xxx Sandstones, coarse
THIRD DIGIT: Degree of consolidation or cementation
1x0xx Totally cemented, dense, hard, unfractured
1x1xx Dense, fractured
1x2xx Well indurated, mod-low porosity (3-10%), unfractured
1x3xx Well indurated, mod-low porosity (3-10%), fractured
1x4xx Well indurated, mod-low porosity (3-10%), highly fractured
1x5xx Indurated, mod-high porosity (>10%), unfractured
1x6xx Indurated, mod-high porosity (>10%), fractured
1x7xx Indurated, mod-high porosity (>10%), highly fractured
1x8xx Poorly indurated, high-v. high porosity, soft
1x9xx Unconsolidated sediment
FOURTH DIGIT: Primary sedimentary structures
1xx0x Vertical perm barriers, shale dikes, cemented vert. fractures
1xx1x Churned/bioturbated to burrow mottled (small scale)
1xx2x Convolute, slumped, large burrow mottled bedding (large scale)
1xx3x Lenticular bedded, discontinuous sand/silt lenses
1xx4x Wavy bedded, continuous sand/silt and mud layers
1xx5x Flaser bedded, discontinuous mud layers
1xx6x Small scale (< 4 cm) x-lam, ripple x-lam, small scale hummocky x-bd
1xx7x Large scale (> 4 cm) trough or planar x-bedded
1xx8x Planar lam, very low angle x-beds, large scale hummocky x-bd
1xx9x Massive, structureless
FIFTH DIGIT: Dominant cementation or pore filling mineral
1xxx0 Sulfide pore filling (RhoG=3.85-5.0)
1xxx1 Siderite (RhoG=3.89)
1xxx2 Phosphate (RhoG=3.13-3.21)
1xxx3 Anhydrite or Gypsum (RhoG=2.98 or 2.35)
1xxx4 Dolomite (RhoG=2.89)
1xxx5 Calcite (RhoG=2.71)
1xxx6 Quartz (RhoG=2.65)
1xxx7 Authigenic clay (RhoG=2.12-2.76)
1xxx8 Carbonaceous debris (RhoG= 2.0)
1xxx9 No pore filling material or detrital clay filled intergranular voids

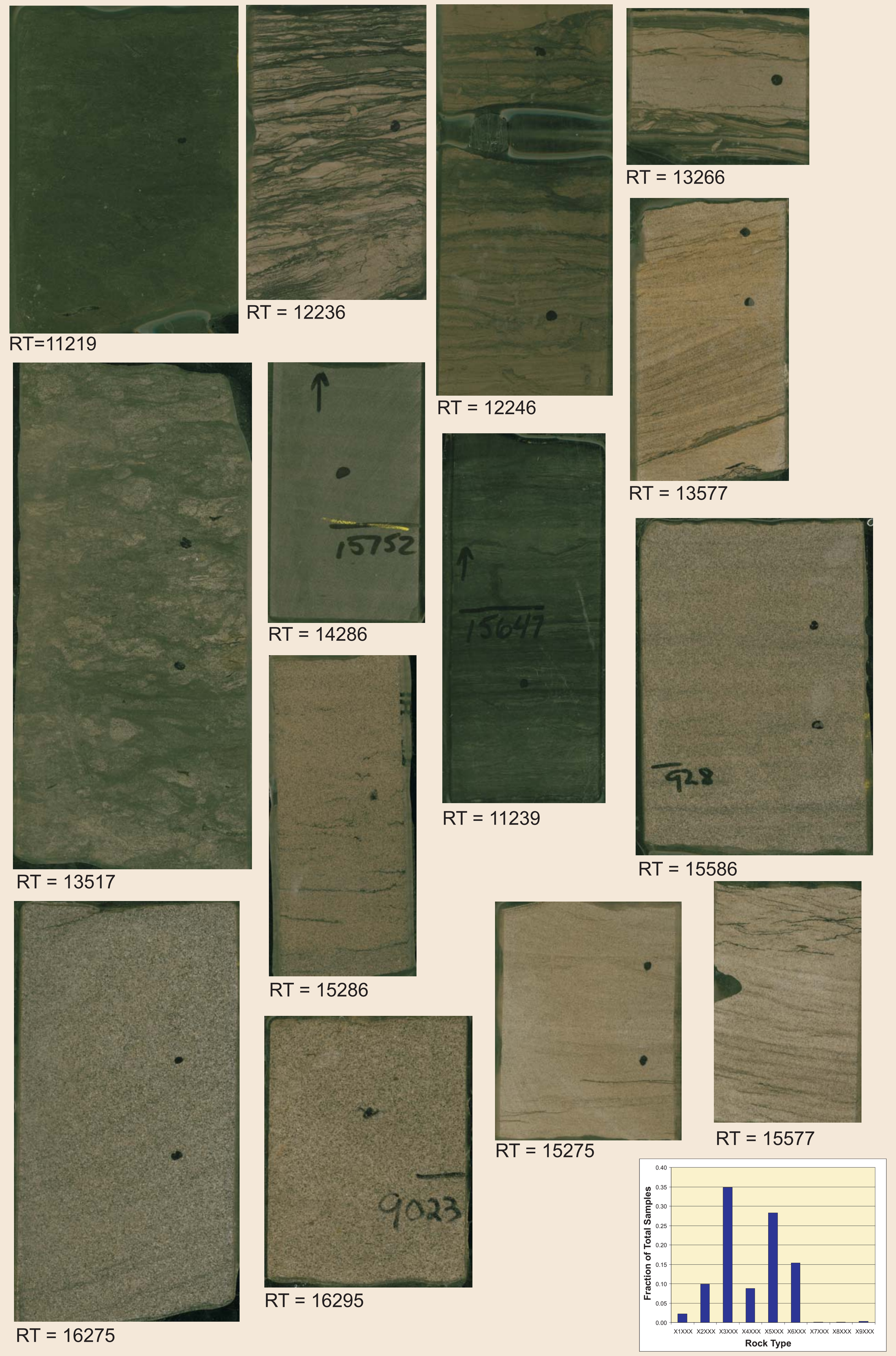

Pore Volume Compressibility

Figure 1 illustrates the pore volume change from 200 psi (1380 kPa) initial confining pressure with increasing confining stress for 113 samples. Every sample exhibited a log-linear relationship between the fraction of initial pore volume (pore volume at 200 psi confining pressure) at confining stress and the confining stress. The average correlation coefficient of the log-linear relationships is 0.99±0.031 (error range is 2 standard deviations).

This log-linear nature of the pore volume change has been previously shown in low-permeability sandstones to characterize crack or sheet-like pore volume compression (Ostensen, 1983). Slopes and intercepts of the curves both increase with increasing porosity (Figures 2 and 3).

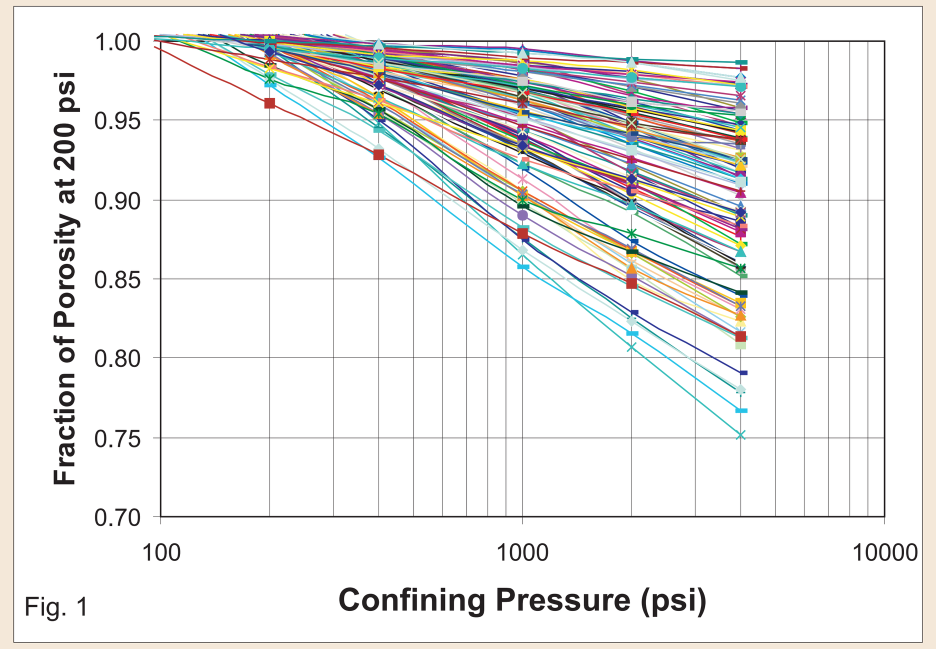

Fig. 1

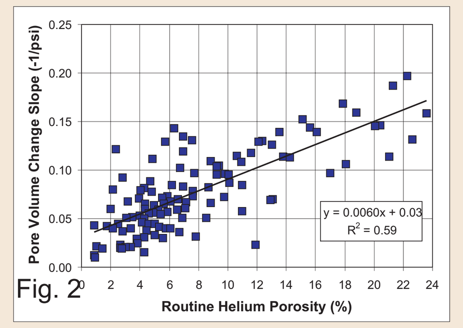

Fig. 2

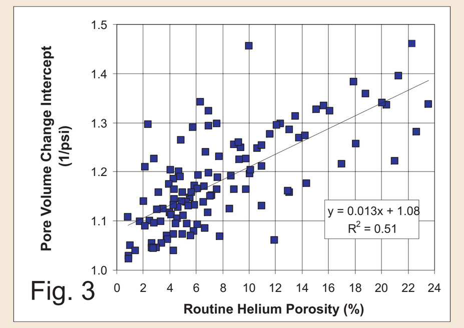

Fig. 3

Utilizing the equations shown in Figures 2 and 3 to calculate slopes and intercepts for rocks of different porosity, the fraction of initial pore volume relationship can be transformed to pore volume compressibility (change in volume/ unit volume/ change in pressure; 1/psi). Figures 4 and 5 show the slope and intercept relationships for prediction of pore volume compressibility of low-permeability sandstones that conform to the equations in Figures 2 and 3.

Combining equations, pore volume compressibility can be predicted for any given Mesaverde low-permeability sandstone with a given porosity at any given net effective confining pressure using:

$\beta = 10\text{\^{}}[(0.000031\phi^2+0.00275\phi-1.016)*\log P+(0.000034\phi^3-0.00223\phi^2+0.056\phi+4.238)]$

Where β is the pore volume compressibility (10^{-6}/psi), P is the average net effective confining pressure at which applies, and ϕ is the unconfined routine porosity (%). This equation predicts that compressibility changes with sandstone porosity and the net effective stress. Figure 6 illustrates general compressibility curves for different porosity sandstones.

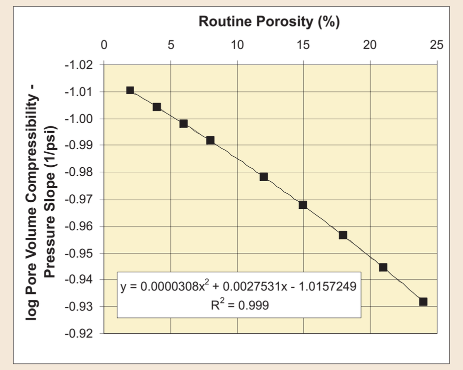

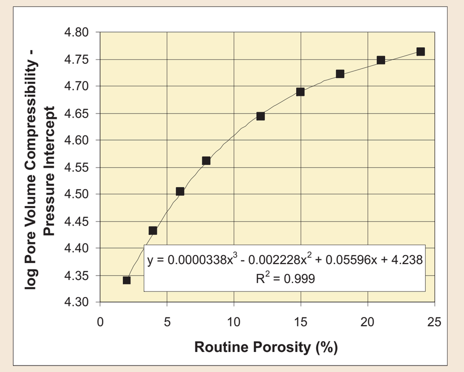

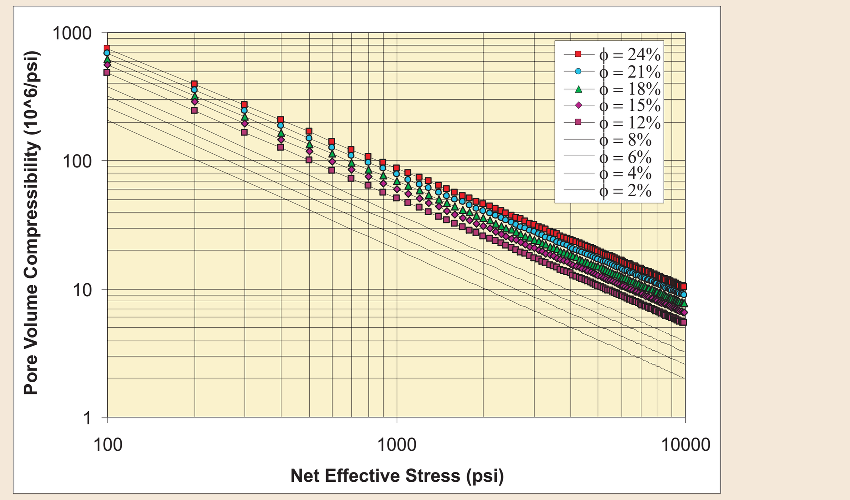

In situ Klinkenberg Permeability vs Routine Air Permeability

Figure 1 shows the Klinkenberg proportionality constant b values measured on core in this study. Reduced major axis analysis predicts a slope and coefficient intermediate between values reported by Jones and Owens (1980) and Heid et al (1950). The b term is expressed in atmospheres. This figure extends the published trend to permeabilities below 0.001 md and supplements the public data for the trend for permeabilities less than 0.01 mD. The variance in b at any given permeability is interpreted to result from several possible conditions including; 1) variance in lithology and corresponding pore throat size and size distribution for the same permeability, 2) heterogeneity of samples resulting in variable b within a sample and resulting averaging of the measured b during measurement, 3) variable b from one end of the sample to the other due to pressure drop across sample, 4) error in one or both gas permeability measurements.

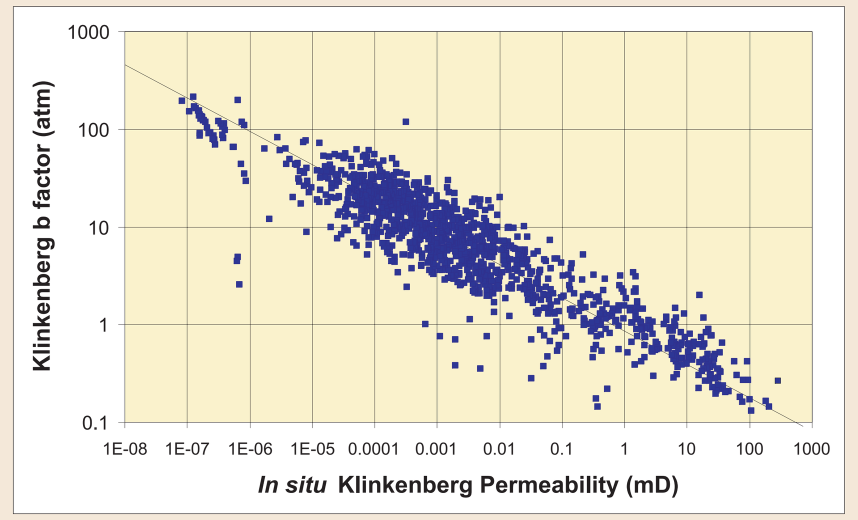

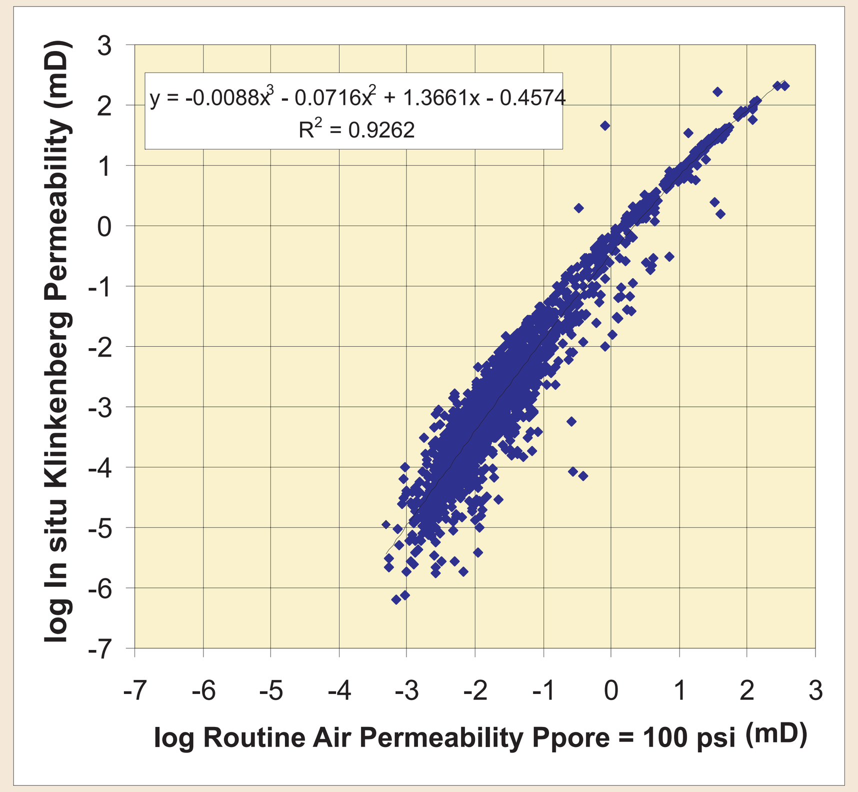

In most low-permeability sandstones, routine air permeability values range from 10 to 1,000 times greater than *in situ* gas and liquid permeability values. Previous studies of low-permeability sandstones have shown that the absolute difference between gas permeabilities measured at routine conditions and those measured under confining stress, both with and without correction for the Klinkenberg gas slippage effect, increases progressively with decreasing permeability and increasing confining stress (Vairogs et al, 1971; Thomas and Ward, 1972; Byrnes et al, 1979; Jones and Owens, 1980; Sampath and Keighin, 1981; Walls et al, 1982; Ostensen, 1983; Wei et al, 1986; Luffel et al, 1991; Byrnes, 1997; Castle and Byrnes, 1998; Byrnes et al, 2001). This relationship can be attributed primarily to the closing of thin, tabular pore throats as confining stress is applied which; 1) is associated with an increase in the Klinkenberg gas slippage factor and a decrease in the Klinkenberg gas permeability, and 2) decreases permeability due to decreasing flow cross-sectional area. Variance is due to several factors including differing rock response to confining stress and differences in mean pore pressure of air permeability measurements.

Comparison of the above equation with the Byrnes (1997) equation:

kik = 10^(1.34 log kair - 0.6)

Shows that the two give statistical similar results for k < 1 mD which is the upper limit for the 1997 equation. The polynomial equation provides prediction for k > 1 mD.

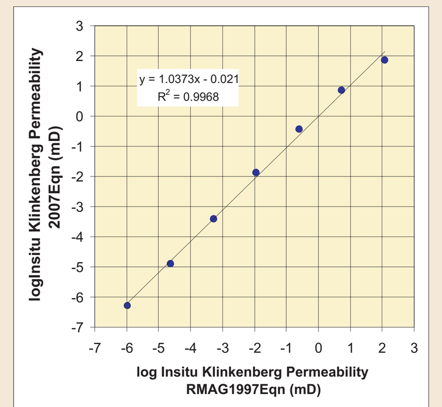

Permeability vs Porosity

Figure 1 illustrates the relationship between permeability and porosity parametric with the second rock classification digit which represents size-sorting. Characteristic of most sandstones, permeability at any given porosity increases with increasing grain size and better sorting though this relationship is further influenced by sedimentary structure (rock digit 4) and the nature of cementation (rock digit 5).

Samples exhibiting permeability greater than the empirically defined high limit generally exhibit an anomalous lithologic property that influences core plug permeability such as microfracturing along a fine shale lamina, a microfracture, lithologic heterogeneity parallel to bedding with the presence of a high permeability lamina in a core plug dominantly composed of a lower permeability-porosity rock. Conversely, cores exhibiting permeability below the lower limit can exhibit such lithologic properties as churned-bioturbated texture, cross-bedding with fine-grained or shaly bed boundaries that are sub-parallel or perpendicular to flow and act as restrictions to flow, or high clay content.

Permeability in low porosity samples and particularly below approximately 1% is generally a complex function of final pore architecture after cementation and is only weakly correlated with original grain size. The estimated range in permeability at any given porosity increases with porosity and can be as great as four orders of magnitude for μ > 12% but decreases to approximately 20X near ϕ=0%. Although in unconsolidated grain packs the influence of size and sorting can be quantified, in consolidated porous media the influence of these variables and particularly the influence of sedimentary structure can be non-linear and non-continuous. For example coarse grain size results in high permeability but if the sand was deposited in a trough cross-bedded structure and there is some orientation of bedding in the core that is not parallel to flow then the permeability can be significantly reduced. The rock classification system used works to both quantify and make continuous these parameters but has limits.

Excluding samples exhibiting permeability outside the limits shown in Figure 1 the relationship between the porosity and lithologic variables and permeability was explored. Multivariate linear regression analysis provides a predictive relationship:

$$\log kik = 0.282\ \phi_i + 0.18\ RC2 - 5.13$$

where kik is the *in situ* Klinkenberg permeability at 4,000 psi net confining stress (mD), ϕi is the *in situ* porosity (%) and RC2 is the second digit of the rock classification representing size-sorting. Standard error of prediction for this equation is a factor of 4.5X (1 standard deviation). Non-linear multivariate regression analysis does not significantly improve predictive capability. The simplest non-linear relation that is not a polynomial that is adjusted to fit the kik-ϕi surface is:

$$\log kik = 0.034\ \phi i^2 - 0.00109\ \phi i^3 + 0.0032\ RC2 - 4.13$$

which exhibits a standard error of prediction of 4.1X (1 std dev).

Because of the non-linear nature of the influence of the independent variable an artificial neural network (ANN) approach was also examined. A single hidden layer, 10 node network was used where the output from the hidden layer was a sigmoidal function (1/1+exp(-x)) of the hidden-layer output. Table 2 shows the ANN parameters. The ANN, using *in situ* porosity (Phii), RC2 and RC4 provides prediction of kik with a standard error of prediction of 3.3X (1 std dev, Fig. 3). These relationships will be explored further when collection of all basic data and rock typing is complete.

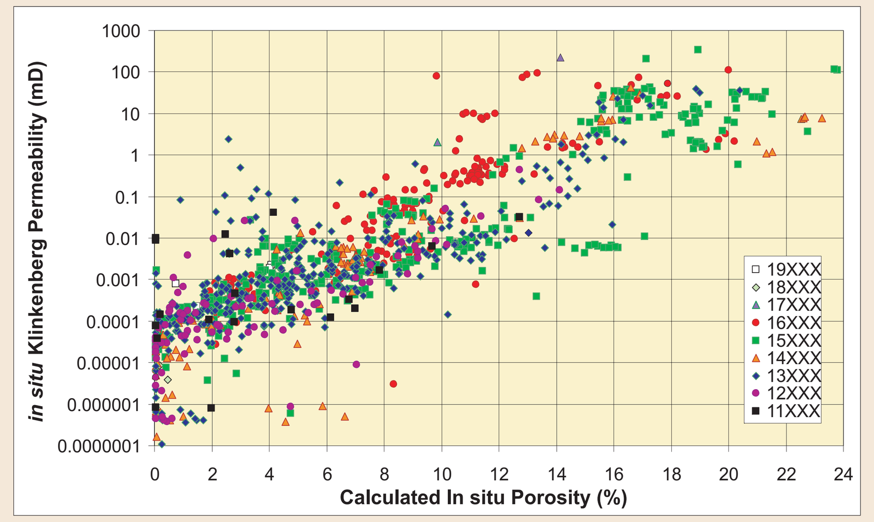

hidden layer: 1
Hidden layer nodes: 10

Node	Constant	Phii	RC2	RC4	hidden layer-to-output weights
Mean>		8.239	4.280	6.294	
Std Dev>		5.260	1.335	2.527	
		Input-to-hidden layer weights			
Constant					-0.388
1	-0.760	2.946	-2.027	-6.438	-0.885
2	-2.155	4.637	1.279	0.895	2.323
3	-4.999	7.901	0.957	3.167	-2.583
4	-1.484	-0.307	-1.695	6.175	-0.154
5	-4.597	4.582	1.568	0.730	4.022
6	-2.609	0.320	-2.201	-2.257	-2.495
7	-1.765	-1.843	-1.122	0.145	-3.859
8	2.839	-3.146	-9.237	0.264	0.789
9	-1.566	1.029	-1.588	-3.390	2.400
10	2.951	0.778	3.316	0.179	-2.136

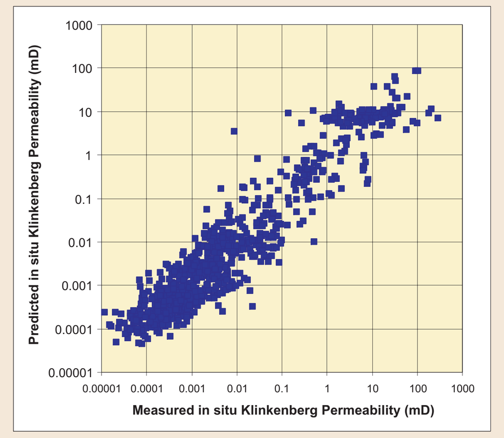

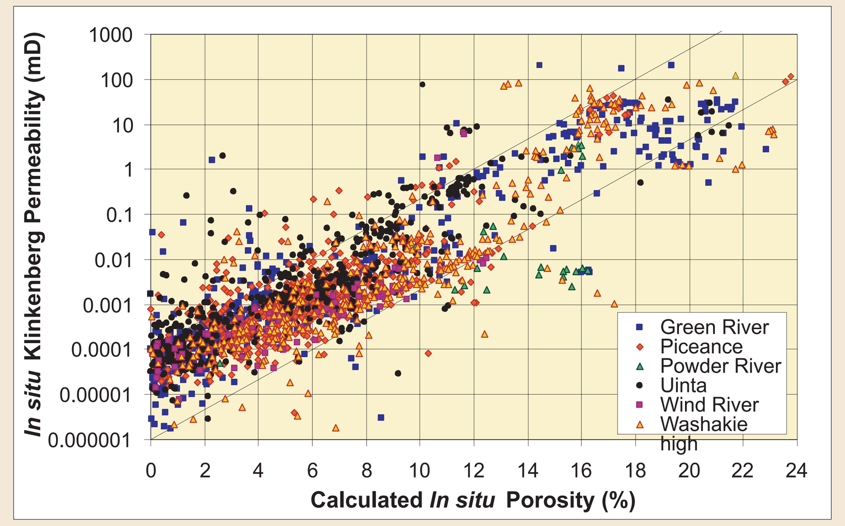

In situ Klinkenberg permeability versus calculated *in situ* porosity by basin. Range of porosity and permeability of Mesaverde sandstones is generally exhibited by all basins. Absence of higher porosity samples for Wind River and Powder River samples is interpreted to be due to sampling and not lack of high porosity rocks in these basins.

In situ and Routine Capillary Pressure

Unconfined and *in situ* (confined) mercury intrusion capillary pressure (MICP) analyses are compared for 73 matched sandstones cores. Two matched core plugs were obtained by cutting a single long core plugs into two plugs of 3-5 cm in length. These sample pairs exhibit an average porosity difference between plug pairs of 0.15±0.3 porosity units (1.8%±3.6% of the average pair porosity) and within a factor of 1.4±2.8 for the *in situ* Klinkenberg permeability (within an average factor of 1.13±2.5 of the average k_{ik}).For *in situ* MICP cores were hydrostatically confined at a pressure of 4,000 psi (27.6 MPa) greater than the mercury injection pressure, maintaining a net effective stress of 4, 000 psi (27.6 MPa). For these analyses the *in situ* pore volume was calculated.

Figure 1 illustrates example unconfined and *in situ* MICP curves for pairs of high- to low-permeability from different wells and basins. Comparison among pairs shows that the diameters associated with the threshold entry pressure decrease with decreasing permeability (Fig. 2). Between core plugs in a pair set several trends are evident. *In situ* and unconfined curves for high-permeability cores (k_{ik} > 1 mD) are nearly identical. With decreasing permeability the difference between unconfined and *in situ* threshold entry pressure increases. For all pairs this difference is greatest at the threshold entry pressure and decreases with decreasing wetting-phase saturation. At wetting phase saturations of 30-50% the *in situ* MICP curve crosses the unconfined curve and exhibits 0-5% lower wetting phase saturation with increasing capillary pressure. MICP curve data are still being analyzed but it can be interpreted that confining stress exerts principal influence on the largest pore throats and that pore throats accessed at non-wetting phase saturations below approximately 50% are not significantly affected by confining stress. This is consistent with these smaller pores comprising pore space within pore bodies or in regions of the rocks where stress is not concentrated.

Fig. 1

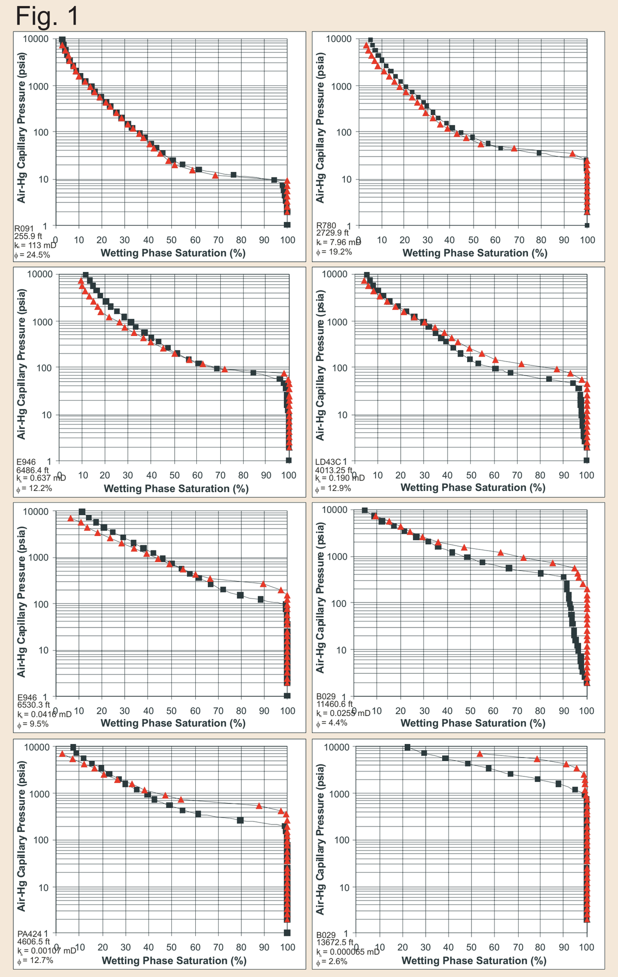

Fig. 2

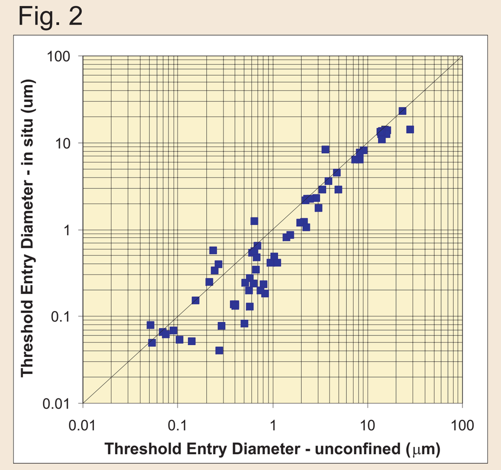

Crossplot of threshold entry pore diameter (A), air-Hg pressure (B), and gas column height (C), measured by MICP versus the ratio of k_{ik}/ϕ_{ik} for in situ data (red triangles), and k_{ik}/ϕ_{ik} for unconfined data (blue squares).

Fig. 4

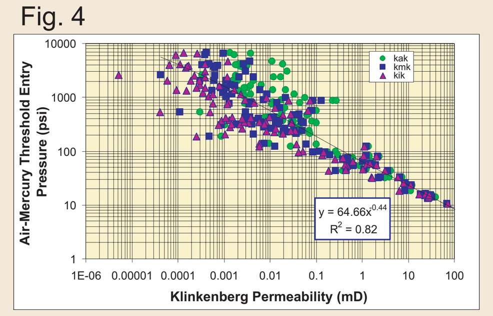

Fig. 3

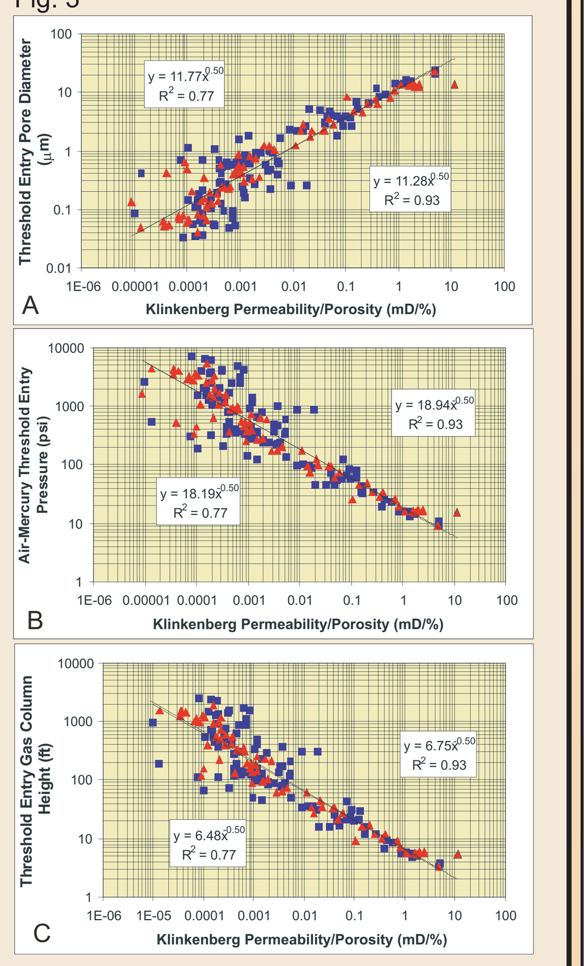

Inputs: P = 2,500-13,000 psia; T = 90-260 °F, 3); ρ_{brine} =1.06±0.05 g/cc; IFT = 47±12 dyne/cm; ρ_{gas} @ P = 0.24±0.12 g/cc.

The compressible nature and the threshold entry pressure of these rocks results in uncertainty for standard unconfined MICP. Up to the threshold entry pressure mercury has not entered the sample and mercury both surrounds the sample and compresses the sample hydrostatically. For sandstones with permeability greater than 0.2 mD the threshold entry pressure of mercury is less than 100 psi (700 kPa) and pore volume compression is less than 1%. However, with decreasing permeability the threshold entry pressure and resulting confining stress increases (Fig. 3) and pore volume decreases. For low-permeability sandstones with k_{ik} < 0.001 mD, confining stress exceeds 1,000 psi (7 MPa) and pore volume is correspondingly an average of 3.5% less than unconfined conditions. With step-wise increase in injection pressure and confining stress for uninvaded rock volume the net effective stress on the uninvaded rock continually changes while invaded portions are decompressed.

The permeability that most closely corresponds to the stress conditions of the unconfined MICP is a Klinkenberg permeability measured at the threshold entry pressure (P_{te}) measured immediately prior to MICP analysis. This permeability is intermediate between the initially measured routine and *in situ* Klinkenberg permeabilities.

Figure 4 illustrates the relationship between unconfined P_{te} and routine, *in situ* and mean permeabilities and shows that the mean permeability exhibits the same relationship as the *in situ* MICP for which these stress issues do not exist. Figure 4 illustrates the good correlation between the threshold entry pore size (and corresponding pressure or gas column height) and permeability. The slope of this relationship is statistically identical for both unconfined and confined conditions because the abscissa represents each set of conditions. Unconfined samples exhibited higher permeabilities and larger threshold entry pore diameters. With application of confining stress the permeability decreased due to the decrease in pore throat diameter. The slope of the relationship between pore size and permeability, 0.5, is the same as the scaling parameter proposed by Leverett (1941) who proposed normalizing capillary pressure using $(k/\phi)^{0.5}$. Because permeability is well correlated with threshold pore throat size it can be used to correct unconfined capillary pressure curves to *in situ* conditions.

The results presented here indicate that capillary pressure measurements on low-permeability sandstones are significantly influenced by confining stress, consistent with observed permeability changes.

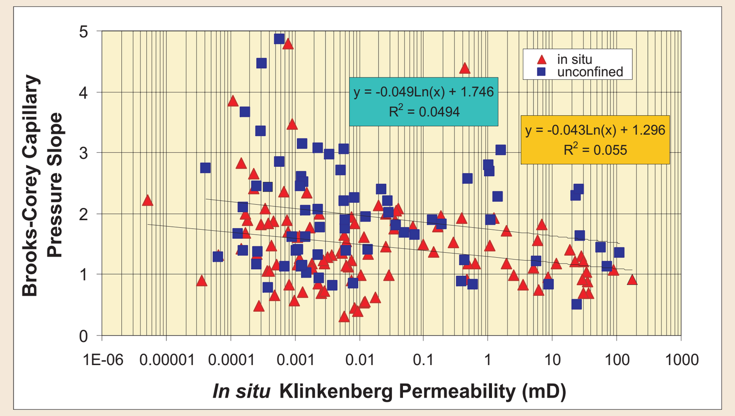

Confining stress decreases pore throat size distribution - comparison of the Brooks-Corey slopes (logSw-logPc slope) indicate that confining stress decreases the pore size distribution for all permeabilities. The change in pore size distribution with permeability is one cause for variance in the traditional Leverett J function.

For higher permeability rocks the Leverett J function can exhibit a similar J-S_w trend for a wide range of rock permeability. However, in low-permeability rocks the scatter in this relationship can make the use of the J Function impractical. The J function scatter can be attributed to change and variance in the relationship between threshold entry and capillary pressure slope and the Leverett J assumed relationship that this correlates with $(k_{ik}/\mu)^{0.5}$.

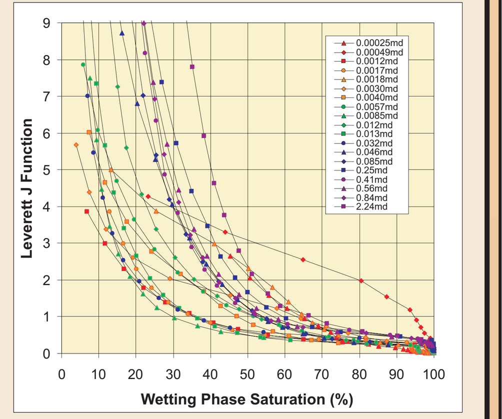

Byrnes, Alan P., John C. Webb, and Robert M. Cluff, 2007, "Regional petrophysical properties of Mesaverde low-permeability sandstones", Proceedings of the American Assoc. Of Petroleum Geologists Rocky Mountain Section Meeting, October 7-9, Snowbird, UT. (Panel 2)

Residual Nonwetting-Phase Saturation

Hysteresis analysis involving three drainage-imbibition cycles for each sample were performed on 32 samples ranging in porosity, permeability, and lithology.. These three cycles represent drainage saturations reaching successively Snw = 0.33±0.15, Snw = 0.57±0.10, and Snw 0.87±0.10. Figure 1 illustrates representative hysteresis curves. As with other samples analyzed, a significant fraction of the trapped non-wetting phase saturation (Snw) results from the early intrusion at low Snw values. Figure 2 illustrates the relationship between the residual saturation to imbibition and the initial drainage saturation for each cycle. In addition to residual saturation measurements on the 32 hysteresis samples, all MICP samples were weighed following analysis. Residual mercury trapped in the core was determined gravimetrically and residual non-wetting phase saturation calculated. For these samples the initial mercury (nonwetting phase) saturation represented the mercury saturation achieved at 9,300 psi intrusion pressure. This saturation is near, or represents a wetting phase saturation less than, "irreducible" saturation. Figure 3 illustrates the relationship between residual nonwetting phase saturation and the initial nonwetting phase saturation for the hysteresis and the single-cycle unconfined MICP samples. The relationship between initial and residual nonwetting phase saturation was characterized by Land (1971) for strongly wet samples:

$$1/Snwr^{*} - 1/Snwi^{*} = C \qquad (1)$$

Where Snwr* = Snwr/(1-Swirr) and Snwi* = Snwi/(1-Swirr).

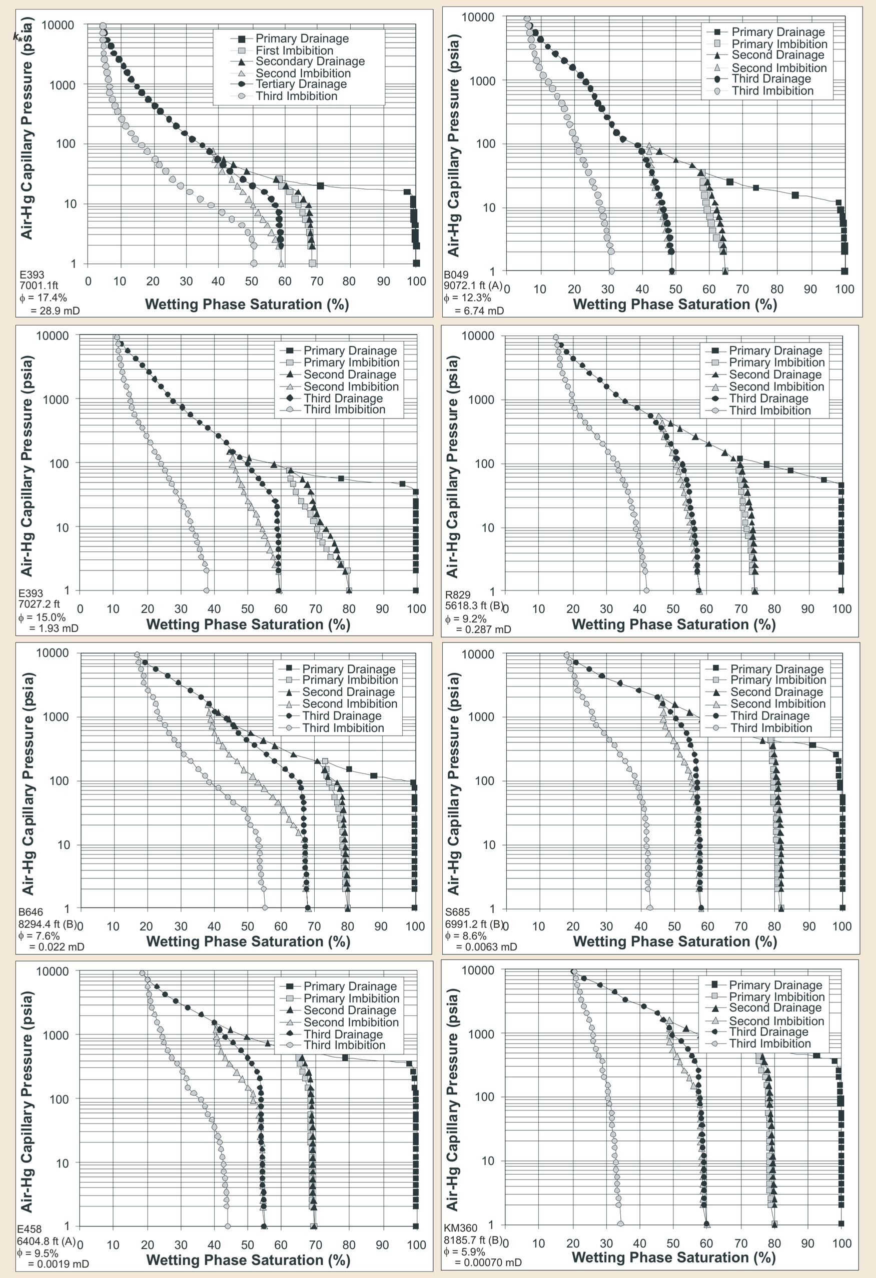

Fig. 1

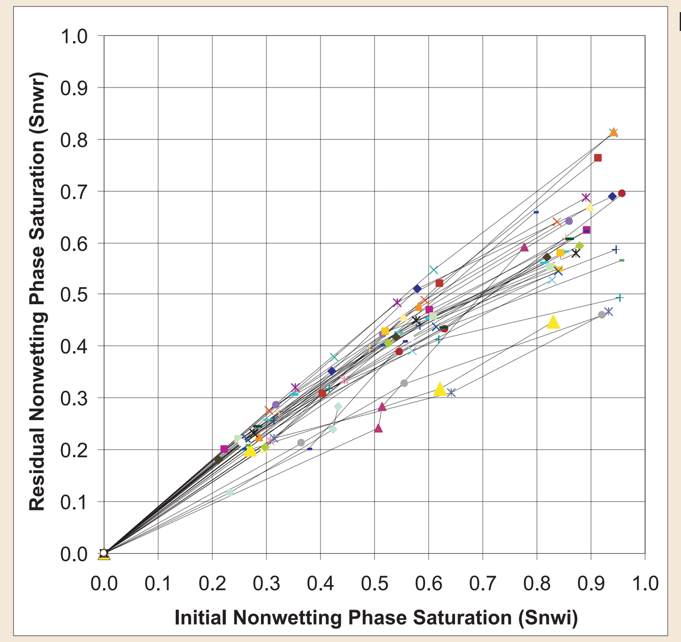

Fig. 2

Sample Condition	Swirr definition	Land C Minimum Error	Snwr Standard Error	Snwr Standard Error
all	Swirr = 1-Snwmax	0.53	0.077	0.077
unconfined	Swirr = 1-Snwmax	0.59	0.087	0.088
hysteresis	Swirr = 1-Snwmax	0.51	0.056	0.057
confined	Swirr = 1-Snwmax	0.45	0.088	0.085
all	Swirr = 0	0.63	0.073	0.073
unconfined	Swirr = 0	0.71	0.080	0.081
hysteresis	Swirr = 0	0.59	0.057	0.057
confined	Swirr = 0	0.54	0.078	0.078
all	Swirr = 0, Snwi<70%	0.70	0.054	0.053
unconfined	Swirr = 0, Snwi<70%	0.83	0.062	0.061
hysteresis	Swirr = 0, Snwi<70%	0.70	0.052	0.051
confined	Swirr = 0, Snwi<70%	0.50	0.038	0.039

Three different measurement populations are compared; unconfined, unconfined with hysteresis, and confined. Unconfined with hysteresis are separated from the unconfined because the hysteresis samples have data for measurements at Sw < Swirr except for the third and last hysteresis drainage-imbibition cycle. Confined samples are samples for which capillary pressure analysis was performed with the sample under a net confining stress of 4,000 psi (27.5 MPa). Table 1 compares Land C values for the different sample populations with Swirr defined as either equal to the minimum saturation achieved in the MICP analysis (Swirr = 1-Snwmax) or Swirr equal to zero (Swirr = 0). The average Land C values represent the average of individual C values calculated for each sample. The Land C Minimum Error values represent the C values that provide a minimum error for all samples in a given population using a single C value.

Optimum prediction of Swnr is obtained using Swirr = 0 rather than Swirr = 1-Swmin. Although the Land C values appear to vary widely, resulting predicted residual saturation values are not highly sensitive for the range of C values exhibited. Iterative solution indicates that C = 0.55 results in the minimum error in residual saturation for all populations with Swirr = 0. Using C = 0.55 the resulting error in Snwr prediction is only 0.001±0.0015 different from the standard error values obtained using C value that provide the minimum error for each population (Table 1). Figure 3 illustrates initial (Snwi) and residual nonwetting phase saturations (Snwr) for the unconfined MICP samples, for which Swirr = 1- Snwmax, and the unconfined hysteresis samples, for which 2 of 3 Swirr < 1- Snwmax. Trapping is slightly greater in the hysteresis samples.

Comparing the residual and initial saturations for unconfined and confined samples (Figure 4) shows that confined samples exhibit greater residual saturation than unconfined with C = 0.54 and C = 0.66 for confined and unconfined (including unconfined and unconfined hysteresis samples), respectively. Greater trapping in confined samples may be the result of a change in the pore body pore throat relationship due to confining stress or it may be the result of the limit placed on exit boundary conditions. Unconfined samples allow mercury to exit the sample from all sides whereas confined samples only allow mercury to exit from one entry face. Assuming a constant number of exit paths in any given direction and the same snap-off conditions, a decrease in the number of exit paths is likely to increase the nonwetting phase volume behind junctions undergoing snap-off in one direction. This change in boundary conditions would likely result in some additional trapping. Whether the increase in residual nonwetting phase saturation is the result of confining stress effects or the difference in boundary conditions is being investigated.

Prediction of Snwr using C = 0.55 and Swirr = 0 appears to provide minimum error for the range of possible measurement condition populations. Utilization of C values specific for a population results in improvement in prediction that is generally less than 2% of Snwr.

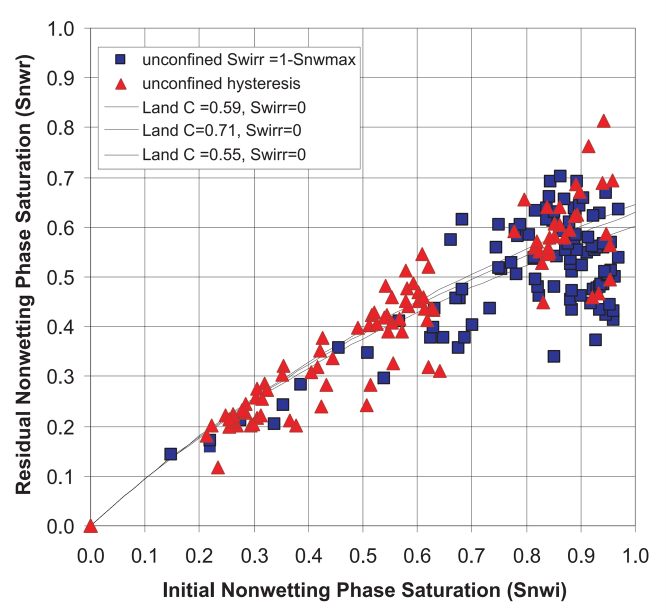

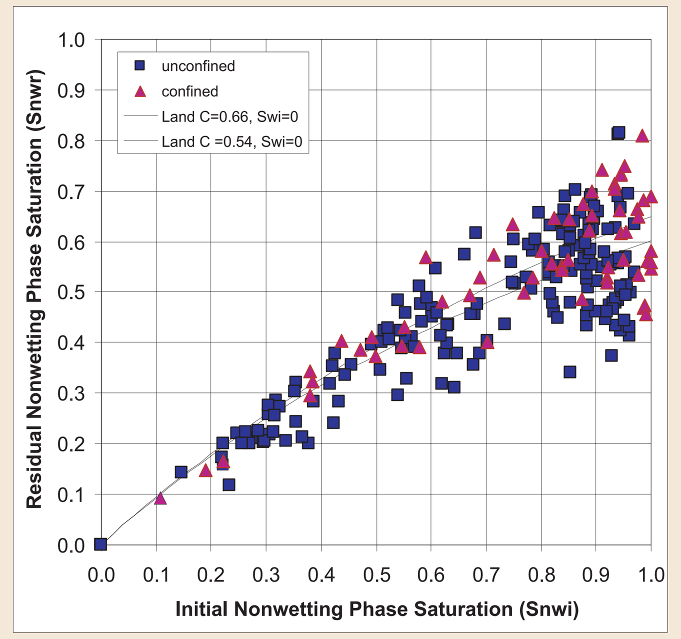

Critical Gas Saturation

Review of gas relative permeability (k_{rg}) studies of low-permeability sandstones indicates they can be modeled using the Corey equation, but scarce data near the critical-gas saturation (S_{gc}) limit k_{rg} modeling at high water saturations. Confined mercury injection capillary pressure and coupled electrical resistance measurements on Mesaverde sandstones of varied lithology were used to measure critical non-wetting saturation. Most of these data support the commonly applied assumption that $S_{gc} < 0.05$. However, a few heterolithic samples exhibiting higher S_{gc} indicate the dependence of S_{gc} on pore network architecture. Concepts from percolation theory and upscaling indicate that S_{gc} varies among four pore network architecture models: 1) percolation (N_p), 2) parallel ($N_{//}$), 3) series (N), and 4) discontinuous series (N_d). Analysis suggests that S_{gc} is scale- and bedding-architecture dependent in cores and in the field.

The models suggest that S_{gc} is likely to be very low in cores with laminae and laminated reservoirs and low (e.g., $S_{gc} < 0.03$-0.07 at core scale and $S_{gc} < 0.02$ at reservoir scale) in massive-bedded sandstones of any permeability. In cross-bedded lithologies exhibiting series network properties, S_{gc} approaches a constant reflecting the capillary pressure property differences and relative pore volumes among the beds in series. For these networks S_{gc} can range widely but can reach high values (e.g., $S_{gc} < 0.6$). Discontinuous series networks, representing lithologies exhibiting series network properties but for which the restrictive beds are not sample-spanning, exhibit S_{gc} intermediate between N_p and N networks.

Consideration of the four network architectures lends insight into the complications of heterogeneous lithologies at differing spatial scales and underscores the difficulty of upscaling laboratory-derived relative permeabilities for reservoir simulation. Analysis also indicates that for some architectures capillary pressure and relative permeability anisotropy may need to be considered.

Percolation and Critical Saturation

Wilkinson and Willemsen (1983) showed that the volume fraction of the percolation threshold, equivalent to S_{gc}, scales with network dimension, L, as:

$$S_{gc}(L) = A\,L^{D-E}$$

where A is a numerical constant, D is the mass fractal dimension of the percolation cluster (D = 1.89 for 2-D, D = 2.52 for 3-D), E is the Euclidean dimension (E = 2 for 2-D and E = 3 for 3-D). For a simple 3-D cubic network A ≈ 0.65. This relation indicates that as $L \infty S_{gc}$ 0 (e.g., S_{gc} = 0.215 for L = 10; S_{gc} = 0.024 for L = 1,000; S_{gc} = 0.008 for L = 10,000).

Pore Networks and k_{rg}, S_{gc}

Pore networks can be broadly classified as exhibiting three end-member architectures and an important intermediate architecture: 1) Percolation network (N_p)- random orientation of pore sizes within the network, 2) Parallel network ($N_{//}$)- preferential orientation of pore sizes or beds of different N_p networks parallel to the invasion direction, 3) Series network (N) - preferential sample-spanning orientation of pore sizes or beds of different N_p networks perpendicular to the invasion direction, and 4) Discontinuous series network (N_d) - preferential non-sample-spanning orientation of pore sizes or beds of different N_p networks perpendicular to the invasion direction (Figure 2). Different sandstone lithologies and the four pore-networks and their relationship to S_{gc} and k_{rg} is discussed. Gas is used as the invading phase for the following discussion.

Percolation Network (N_p)

A massive-bedded or uniformly bioturbated sandstone, siltstone, or shale might exhibit a pore network that can be represented by a percolation network. For this network, formation of the percolation cluster would occur at $S_g < 0.03$-0.07 at the core-plug scale and would approach $S_{gc} < 0.01$-0.02 at large scales following Equation 2. Massive-bedded sandstone and siltstone is a common lithology in low-permeability sandstones and therefore low S_{gc} is likely to be common in many reservoir systems.

Parallel Network ($N_{//}$)

Planar- and horizontally-laminated bedding is common in marine and tidal flat environments. In addition, many sedimentary structures that might be Series Networks on a large scale can exhibit $N_{//}$ properties at smaller scales including core scale. Parallel networks perform similarly to percolation networks except that portions of the network are not involved in the invasive flow associated with establishing S_{gc}.

The presence of a single, sample-spanning, one-millimeter-thick lamina in a core, even with high $S_{gc,low}$, can result in a very low S_{gc} value for the core (e.g., a lamina with $S_{gc,low}$ = 0.5, representing 1% of the total core volume, results in a core S_{gc} = 0.005). Frequently, core sampling procedures avoid sampling series flow architecture by orienting plugs parallel to bedding, thereby creating a sample with $N_{//}$ properties.

Series Network (N)

Sedimentary bedding structures that represent series networks in one or more dimensions at one or more scales are abundant in nature (e.g., trough cross-bedding, large- and small-scale planar cross-bedding, low-angle planar bedding, hummocky bedding, Flaser bedding). Within these structures scales of series networks range from millimeter-scale laminae to decameter scale cross-bedding. If the continuity of the beds is broken such that the beds are not sample-spanning then the series network is discontinuous as discussed below.

In a N network, percolation across the system does not occur until the invading gas pressure equals or exceeds the threshold pressure ($Pc_{Sgc,high}$) required to achieve critical saturation in the single barrier-bed with the highest pressure needed to allow percolation through that barrier-bed ($S_{gc,high}$):

$$S_{gc} = [(S_{g,Pc\text{-}Sgc,high})_i \mu_i V_i] / [\mu_i V_i]$$

Figure 4 illustrates a simple cross-bedded system consisting of two lithologies that exhibits very high S_{gc} as a result of the significant difference in the capillary pressure properties of the beds (e.g., siltstone laminae within sandstone). Corey and Rathjens (1956) observed critical-gas saturations of 0.60 in a cross-bedded sandstone with flow perpendicular to bedding.

$S_{gc,high}$ for the most-restrictive barrier-bed can be considered to follow Equation 7 and approaches zero at infinite size. However, the system S_{gc} does not approach zero but approaches a constant

It is important to note that most reservoir-, flow-simulation software treat capillary pressure and relative permeability as scalars and do not provide directional components (e.g., krg_x, krg_y, Pc_x, etc.) as they do for permeability (e.g., k_x, k_y, k_z)

Discontinuous Series Network (N_d)

The N network discussed above requires that the barrier-beds be sample-spanning perpendicular to the direction of invasion. Beds may not be sample-spanning or may have holes. These represent discontinuous series networks (N_d) and represent a continuum between a Percolation, N_p, and a Series, N, network. Fundamentally, since a continuous path across the system exists through the "host" network, S_{gc} in a N_d network follows Equation 2. However, because some potential paths for the sample-spanning cluster are blocked S_{gc} is greater than for a N_p network of the same dimension. Though a formal mathematical analysis is not known, it can be estimated that S_{gc} in a N_d network follows Equation 2 but exhibits a decrease in slope as barrier-beds approach sample-spanning dimensions.

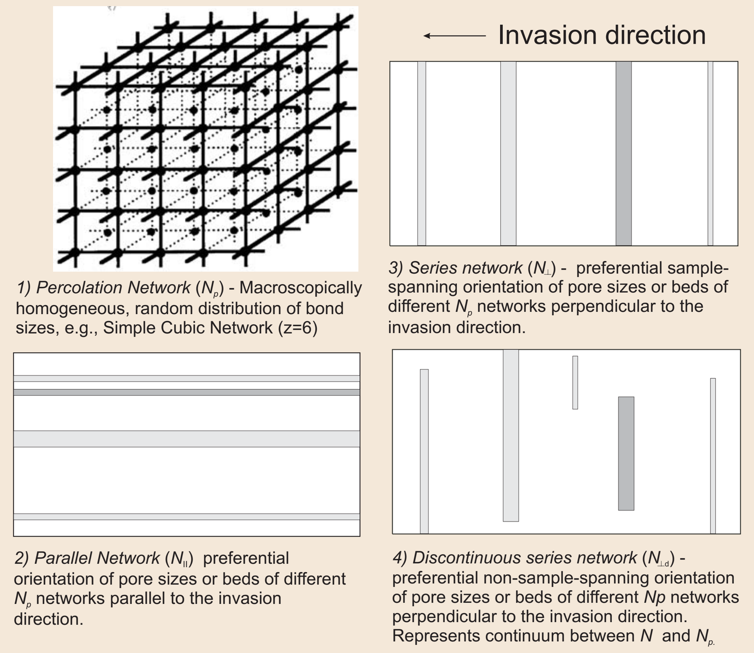

1) Percolation Network (N_p) - Macroscopically homogeneous, random distribution of bond sizes, e.g., Simple Cubic Network (z=6)

3) Series network (N) - preferential sample-spanning orientation of pore sizes or beds of different N_p networks perpendicular to the invasion direction.

2) Parallel Network ($N_{//}$) preferential orientation of pore sizes or beds of different N_p networks parallel to the invasion direction.

4) Discontinuous series network (N_d) - preferential non-sample-spanning orientation of pore sizes or beds of different Np networks perpendicular to the invasion direction. Represents continuum between N and N_p.

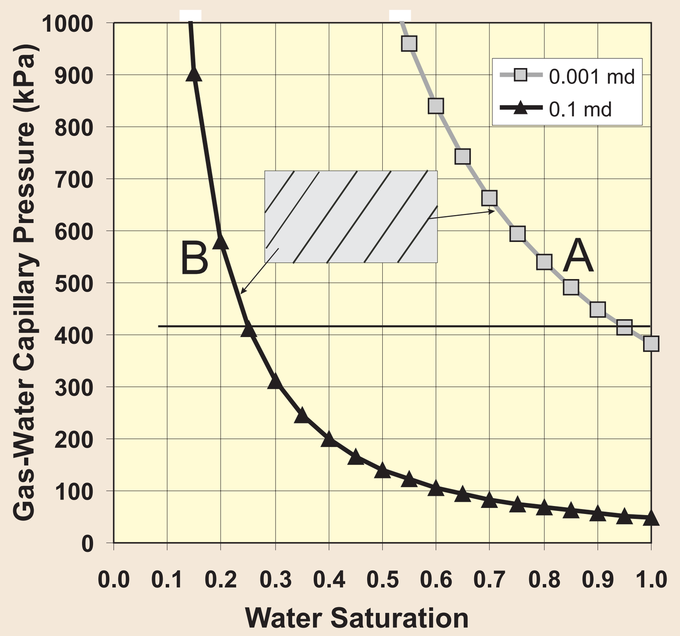

A modified-Corey (1954) equation can be usede to predict gas relative permeability in low-permeability sandstones:

$$k_{rg} = (1\ \ (S_w - S_{wc,g})/(1 - S_{gc} - S_{wc,g}))^p\ (1 - ((S_w - S_{wc,g})/(1 - S_{wc,g}))^q)$$

Though there is scatter, interpreted to primarily represent pore architecture variation in rocks of different lithofacies, for both the complete k_{rg} curves and the composite individual $k_{rg,Sw}$ measurements there is a general trend that at any given water saturation the gas relative permeability of lower permeability samples is less than that of higher permeability samples. Byrnes (2003) empirically fit the data in Figure 1 to Equation 1 using:

$$S_{wc,g} \approx 0.16 + 0.053 * \log_{10} k_{ik} \quad (\text{for } k_{ik} \geq 0.001 \text{ mD})$$
$$S_{wc,g} = 0 \quad (\text{for } k_{ik} < 0.001 \text{ mD})$$
$$S_{gc} \approx 0.15 - 0.05 * \log_{10} k_{ik}$$
$$p = 1.7$$
$$q = 2$$

These empirical equations were interpreted to be consistent with previously published parameters and to bracket existing data and approximately model the parametric relationship with absolute permeability.

Figure 3 shows the same bounding k_{rg} curves as Figure 1 but extended to high S_w and low k_{rg} values. The bounding black curves were constructed using the equations for rocks of 0.001 millidarcies (mD; 1 mD = 0.000987 μm^2) and 1 mD, where S_{gc} = 0.3 for k_{ik} = 0.001 mD and S_{gc} = 0.15 for 1 mD, and p = 1.7, q = 2. The bounding dark grey curves illustrate a match for the data but with a constant S_{gc} = 0.01 and with the exponent p varying with absolute permeability and q = 2; e.g., p = 2.9 for k_{ik}= 0.001 mD and p = 2 for k_{ik} = 1 mD, respectively. Within the relative permeability range of most of the measured data (S_w<0.6), k_{rg} can be modeled equally well by holding S_{gc} constant and expressing $p(k)$ or setting p constant and expressing $S_{gc}(k)$. However, at S_w > 0.6 the variable p/constant low-S_{gc} model ($p(k)$; S_{gc}<0.05) exhibits significantly higher k_{rg} values than the constant p/variable S_{gc} model (p≈C; $S_{gc}(k)$).

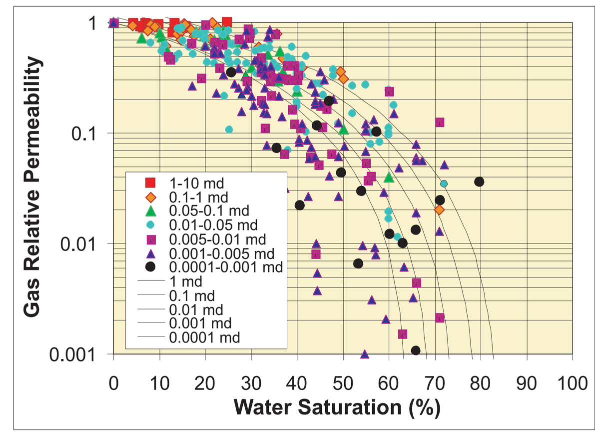

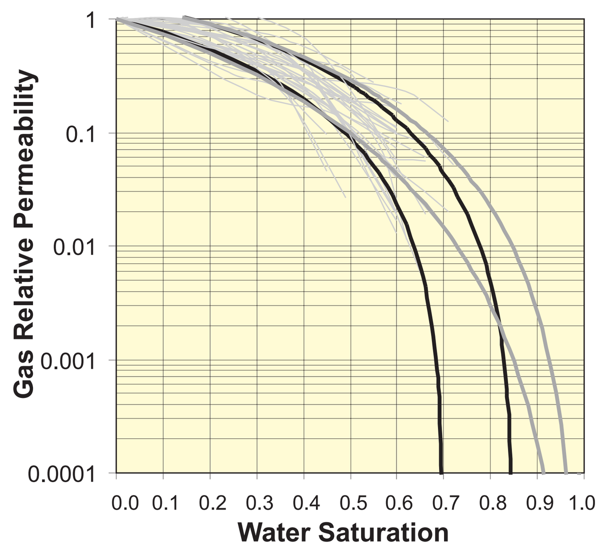

Analysis of *in situ* mercury intrusion capillary pressure (MICP) for critical nonwetting phase saturation was performed using both MICP inflection analysis and electrical resistance analysis. Resistance across the core was measured using stainless steel electrodes on each end of the core (Figure 1). At the critical saturation of the percolation threshold, with formation of a continuous mercury tendril across the sample, resistance across the core decreases abruptly by one-third to five orders of magnitude. From each sample's capillary pressure curve the saturation associated with the characteristic length, l_c, as defined by Thompson et al. (1987), was measured at the first inflection point.

Figure 2 illustrates the relationship between S_{nwc} and permeability, as measured by the inflection point and electrical resistance on the 70 confined MICP samples. As measured by MICP curve inflection, average confined S_{nwc} = 0.028 ±0.046 for rocks with k_{ik} > 0.01 mD and average S_{nwc} = 0.048 ± 0.096 for rocks with $k_{ik} \leq$ 0.01 mD (error bars represent two standard deviations). As measured by increase in electrical resistance, average confined S_{nwc} = 0.043 ±0.11 for rocks with k_{ik} > 0.01 mD and average S_{nwc} = 0.078 ± 0.2 for rocks with $k_{ik} \leq$ 0.01 mD (error bars represent two standard deviations).

For 43% of the samples, the inflection-interpreted S_{nwc} corresponds to the mercury saturation (S_{Hg}) above which electrical resistance across the core exhibits values greater than 0.15-4 x 10^6 ohms and below which resistance values are less than 5-50 ohm, a decrease of more than four- to six-orders of magnitude. This is interpreted to result from formation of a highly-conductive continuous path of mercury through the sample. For an additional 25% of the samples the interpreted S_{nwc} corresponded to a decrease in resistance of greater than 1.5 standard deviations of the average of the previous five resistance measurements, interpreted to result from formation of a continuous mercury path of limited volume and high tortuosity. From these results, for 68% of the samples the inflection and the resistance measurements can be interpreted to agree on the interpreted critical saturation. Within this population, average S_{nwc} = 0.036±0.08 with a maximum value of S_{nwc} = 0.175. The remaining 32% of samples did not exhibit a resistance decrease until mercury saturation increased an additional S_{Hg}= 0.03-0.29 (average S_{Hg} = 0.13), corresponding to mercury saturations of S_{Hg}= 0.02-0.42 (average S_{Hg} = 0.16). For these 32% of samples the inflection S_{nwc} is interpreted to represent "pretender" clusters in a series network and the resistance-interpreted S_{nwc} provides a measure of the sample-spanning S_{nwc}.

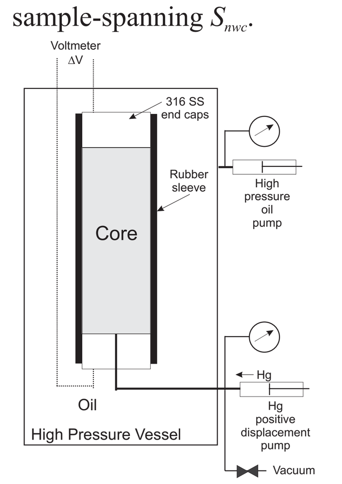

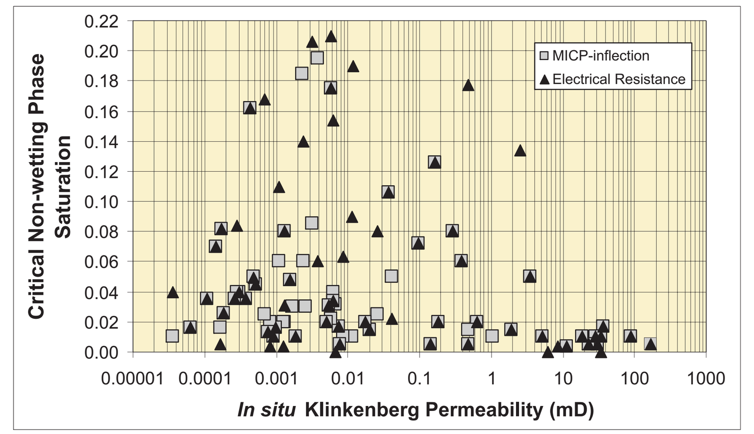

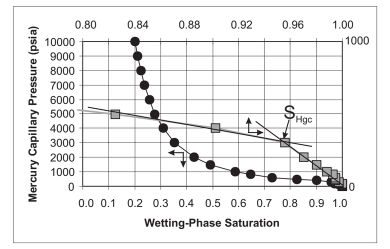

Archie Cementation Exponent

Electrical resistivity analysis for 200,000 ppm NaCl brine, performed on 287 samples of varied lithology and porosity, indicates that the Archie cementation exponent, *m*, decreases with decreasing porosity. Multisalinity measurements to obtain salinity independent electrical properties are being conducted. The data shown represent final high salinity analyses.

Final analysis is waiting on other salinity measurements but the present data can be modeled either empirically or with a dual porosity model (Serra, 1989). Empirically the data can be modeled using a polynomial:

$$m = 0.95 - 9.2\phi + 6.35\phi^{0.5} \text{ (magenta curve)}$$

The dual porosity model for a fractured reservoir or a reservoir with touching vugs represents the conductivity as two circuits in parallel and can be represented by:

$$m = \log[(\phi - \phi_2)^{m1} + \phi_2^{m2}]/\log\phi$$

Where ϕ = bulk porosity
- ϕ_2 = fracture or touching vug porosity
- m_1 = matrix cementation exponent
- m_2 = fracture or touching vug cementation exponent

In the figure the bulk cementation data rare approximately bracketed by for the following conditions:

High:	$m_1 = 2.1$, $\phi_2 = 0.0005$, $m_2 = 1$
Intermediate:	$m_1 = 2.0$, $\phi_2 = 0.001$, $m_2 = 1$
Low:	$m_1 = 1.8$, $\phi_2 = 0.002$, $m_2 = 1$

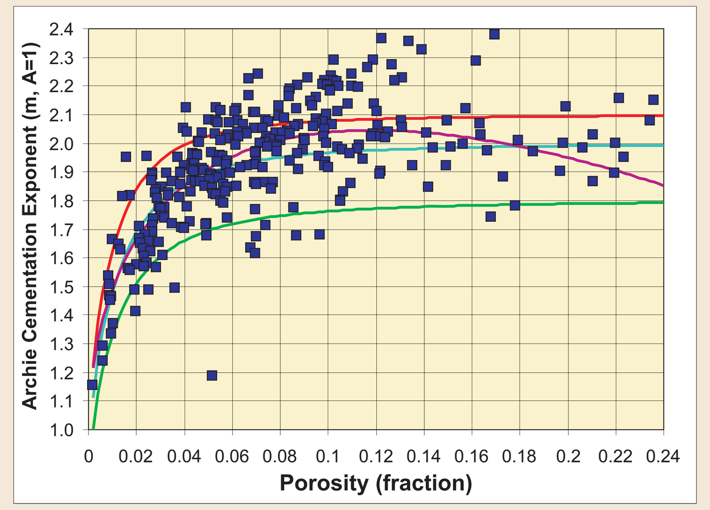

Thin section preparation of low-permeability sandstones has always been hampered by the inability to efficiently impregnate sandstone samples with blue dye epoxy because of the low permeability and the consequent inability to flow epoxy deeply enough into the sample. Most commercial epoxies have an viscosity of ~100 centipoise (cp) and a pot life of ~30 minutes. Calculations indicate that for the standard pot life of 30 minutes (1800 seconds), epoxy penetrates less than 0.27 mm into rocks of less than 0.1 mD. This would indicate that for most low-permeability sandstones the standard impregnation technique does not prove thin sections with blue dye epoxy in the pore space. Even with high-pressure impregnation, where conventionally the samples are placed in a gas pressure vessel an exposed to a gas pressure over the epoxy covering the sample of approximately 1,500 psi (10.3 MPa), impregnation is less than 1 mm for samples with permeability less than 0.01 mD.

Experiments on Mesaverde sandstone samples found that good impregnation was achieved using an extended pot-life viscosity with moderate pressure - EPO-TEK 301-2FL.

Applied Pressure psi	Capillary force psi	Total pressure psi	Permeability mD	Epoxy Impregnation Depth (mm) time (min) 2	time (min) 4	time (min) 8	time (min) 10	time (min) 20	time (min) 30	time (min) 300	time (min) 600
14.7	0.3	15	1000	1.25E+01	1.25E+01	1.25E+01	1.25E+01	1.25E+01	1.25E+01	1.25E+01	1.25E+01
14.7	0.7	15	100	1.01E+01	1.25E+01	1.25E+01	1.25E+01	1.25E+01	1.25E+01	1.25E+01	1.25E+01
14.7	1.9	17	10	1.08E+00	2.17E+00	4.33E+00	5.41E+00	1.08E+01	1.25E+01	1.25E+01	1.25E+01
14.7	4.9	20	1	1.28E-01	2.57E-01	5.13E-01	6.41E-01	1.28E+00	1.92E+00	1.25E+01	1.25E+01
14.7	13.0	28	0.1	1.81E-02	3.62E-02	7.23E-02	9.04E-02	1.81E-01	2.71E-01	2.71E+00	5.43E+00
14.7	17.4	32	0.05	1.05E-02	2.10E-02	4.19E-02	5.24E-02	1.05E-01	1.57E-01	1.57E+00	3.14E+00
14.7	34.2	49	0.01	3.19E-03	6.38E-03	1.28E-02	1.60E-02	3.19E-02	4.79E-02	4.79E-01	9.58E-01
14.7	45.7	60	0.005	1.97E-03	3.95E-03	7.89E-03	9.87E-03	1.97E-02	2.96E-02	2.96E-01	5.92E-01
14.7	89.9	105	0.001	6.83E-04	1.37E-03	2.73E-03	3.42E-03	6.83E-03	1.02E-02	1.02E-01	2.05E-01
14.7	120.3	135	0.0005	4.41E-04	8.81E-04	1.76E-03	2.20E-03	4.41E-03	6.61E-03	6.61E-02	1.32E-01
147	0.3	147	1000	1.25E+01	1.25E+01	1.25E+01	1.25E+01	1.25E+01	1.25E+01	1.25E+01	1.25E+01
147	0.7	148	100	1.25E+01	1.25E+01	1.25E+01	1.25E+01	1.25E+01	1.25E+01	1.25E+01	1.25E+01
147	1.9	149	10	9.72E+00	1.25E+01	1.25E+01	1.25E+01	1.25E+01	1.25E+01	1.25E+01	1.25E+01
147	4.9	152	1	9.92E-01	1.98E+00	3.97E+00	4.96E+00	9.92E+00	1.25E+01	1.25E+01	1.25E+01
147	13.0	160	0.1	1.04E-01	2.09E-01	4.18E-01	5.22E-01	1.04E+00	1.57E+00	1.25E+01	1.25E+01
147	17.4	164	0.05	5.37E-02	1.07E-01	2.15E-01	2.68E-01	5.37E-01	8.05E-01	8.05E+00	1.61E+01
147	34.2	181	0.01	1.18E-02	2.37E-02	4.73E-02	5.92E-02	1.18E-01	1.77E-01	1.77E+00	3.55E+00
147	45.7	193	0.005	6.29E-03	1.26E-02	2.52E-02	3.15E-02	6.29E-02	9.44E-02	9.44E-01	1.89E+00
147	89.9	237	0.001	1.55E-03	3.09E-03	6.19E-03	7.74E-03	1.55E-02	2.32E-02	2.32E-01	4.64E-01
147	120.3	267	0.0005	8.73E-04	1.75E-03	3.49E-03	4.36E-03	8.73E-03	1.31E-02	1.31E-01	2.62E-01
1470	0.3	1470	1000	1.25E+01	1.25E+01	1.25E+01	1.25E+01	1.25E+01	1.25E+01	1.25E+01	1.25E+01
1470	0.7	1471	100	1.25E+01	1.25E+01	1.25E+01	1.25E+01	1.25E+01	1.25E+01	1.25E+01	1.25E+01
1470	1.9	1472	10	1.25E+01	1.25E+01	1.25E+01	1.25E+01	1.25E+01	1.25E+01	1.25E+01	1.25E+01
1470	4.9	1475	1	9.63E+00	1.25E+01	1.25E+01	1.25E+01	1.25E+01	1.25E+01	1.25E+01	1.25E+01
1470	13.0	1483	0.1	9.68E-01	1.94E+00	3.87E+00	4.84E+00	9.68E+00	1.25E+01	1.25E+01	1.25E+01
1470	17.4	1487	0.05	4.86E-01	9.71E-01	1.94E+00	2.43E+00	4.86E+00	7.29E+00	1.25E+01	1.25E+01
1470	34.2	1504	0.01	9.82E-02	1.96E-01	3.93E-01	4.91E-01	9.82E-01	1.47E+00	1.25E+01	1.25E+01
1470	45.7	1516	0.005	4.95E-02	9.90E-02	1.98E-01	2.47E-01	4.95E-01	7.42E-01	7.42E+00	1.48E+01
1470	89.9	1560	0.001	1.02E-02	2.04E-02	4.07E-02	5.09E-02	1.02E-01	1.53E-01	1.53E+00	3.06E+00
1470	120.3	1590	0.0005	5.19E-03	1.04E-02	2.08E-02	2.60E-02	5.19E-02	7.79E-02	7.79E-01	1.56E+00
				Standard Pot-life						Extended Pot-life	

Draft Conclusions

1) Grain density for 2400 samples averages 2.654±0.033 g/cc (±1sd) with grain density distributions differing slightly among basins.
2) Klinkenberg gas slip proportionality constant, b, can be approximated using the relation: $b(atm) = 0.851\, k_{ik}^{-0.34}$.
3) $\log k_{ik} = 0.282\, \phi_t + 0.18\, RC2 - 5.13$ (±4.5X,1 sd)
4) Artificial neural network analysis provides prediction within ±3.3X
5) Capillary pressure (Pc) exhibits an log-log linear threshold entry pressure (P_{te}) versus k_{ik} and k_{ik}/ϕ_i trend and variable Brooks-Corey slopes.
6) Residual nonwetting-phase saturation to imbibition (*Srnw*) increases with increasing initial nonwetting phase saturation (*Snwi*) consistent with the Land-type relation: 1/Snwr-1/Snwi = 0.55.
7) Critical nonwetting-phase (e.g., gas) saturation is low (Sgc < 0.05) in massive and parallel bedded lithologies but may increase in rocks with more complex bedding Percolation theory provides a tool for predicting limits..
7) Archie cementation exponent (*m*) decreases with decreasing porosity (ϕ) below approximately 0.06 and can be generally described by the empirical relationship: $m = 0.95 - 9.2\,\phi + 6.35\,\phi^{0.5}$ or by a dual- porosity model
8) These relationships are still being investigated. The Mesaverde Project website is (http://www.kgs.ku.edu/mesaverde).

Byrnes, Alan P., John C. Webb, and Robert M. Cluff, 2007, "Regional petrophysical properties of Mesaverde low-permeability sandstones", Proceedings of the American Assoc. Of Petroleum Geologists Rocky Mountain Section Meeting, October 7-9, Snowbird, UT. (Panel 3)